Far and mid-infrared studies of star forming regions

Koumpia, Evgenia

E. Koumpia, D.A. Semenov, F.F.S. van der Tak, A.C.A. Boogert, E. Caux – *"The chemical structure of NGC 1333 IRAS 4A",* To be submitted for publication in Astronomy & Astrophysics

Chapter 5

The chemical structure of NGC 1333 IRAS 4A

> The nitrogen in our DNA, the calcium in our teeth, the iron in our blood, the carbon in our apple pies were made in the interiors of collapsing stars. We are made of starstuff.
>
> Carl Sagan

Abstract

It is not well known what drives the chemistry of a protostellar envelope, in particular the role of the stellar mass and the protostellar outflows on the chemical enrichment of such environments.

We study the chemical structure of the Class 0 protostar NGC 1333 IRAS 4A in order to (i) investigate the influence of the outflows in the chemistry, (ii) constrain the age of our studied object, (iii) compare it with a typical high–mass protostellar envelope. In our analysis we use JCMT mapping observations (360–373 GHz) and HIFI single pointing data (626.01– 721.48 GHz). We first estimate the average excitation temperature and column density that characterize the outflow and the envelope of our source using H_2CO lines, adopting a simple LTE approximation. To study the influence of the outflow on the degree of deuteration, we model our observed JCMT maps with RADEX to produce the DCO^+/HCO^+ in a region that spatially covers the outflow activity of IRAS 4A. Lastly, we derive empirical molecular abundance profiles for the observed species using the Monte Carlo radiative transfer code (RATRAN) and adopting a 1D dust density/temperature profile from the literature. We use a combination of constant abundance profiles and abundance profiles that include jumps at two radii (T∼100 K or T∼30 K) to fit our observations. We compare our best–fit observed abundance profiles with the predictions from the time dependent gas grain chemical code (ALCHEMIC).

We detect CO, ^{13}CO, $C^{18}O$, CS, HCN, HCO^+, N_2H^+, H_2CO, CH_3OH, H_2O, H_2S, DCO^+, HDCO, D_2CO, SO, SO_2, SiO, HNC, CN, C_2H and OCS. The observed abundance profiles for many species are reproduced by a 1D pseudo-time-dependent gas-grain chemical model for the outer envelope, with the exceptions of HCN, HNC, CN. The observed CO abundance requires an enhanced UV field which points towards an outflow cavity. The abundances are 1 to 2 orders of magnitude lower than those

observed in the high mass protostellar envelope (AFGL 2591). This enhancement can be explained by the significant difference on the temperature profiles among low and high mass protostellar envelopes, especially the absence of a freeze–out zone in the high mass case. The CH_3OH modeled abundance profile points towards an age of $\geqslant 4\times10^4$ yrs for IRAS 4A. The spatial distribution of H_2D^+ differs from that of other deuterated species (i.e. DCO^+, HDCO and D_2CO), indicating origin from a colder layer in the foreground.

The observed abundances can be explained by passive heating towards the high mass protostellar envelope, while the presence of UV cavity channels become more important toward the low mass protostellar envelope (e.g. CO, HCO^+.

5.1 Introduction

During low mass (< 2 $M_\odot$) star formation a rotating cloud of gas and dust collapses under gravitational forces. The central protostar increases in mass through the accretion disk that surrounds it. The main mechanisms that retard the gravitational collapse are the thermal pressure, magnetic fields and turbulence (Luhman 2012; Evans 2011; Hennebelle & Motte 2009; Tan 2015). Turbulence can be enriched by energetic outflows from young stellar objects (YSOs) which may further trigger star formation (Quillen et al. 2005).

Molecular outflows are prominent during the earliest stages of star formation, especially when collimated jets are driven in the youngest (10^3–10^4 years) embedded protostars (Arce et al. 2007). Class 0 protostars are still in their main accretion phase and they also drive the most powerful outflows. The impact of the ejected material on the surrounding cloud causes shock fronts. These lead to changes in the chemical composition and the enhancement of the abundance of several species in the surroundings. Fontani et al. (2014a) have found enhancement of HDCO/H_2CO towards the shock location of a Class 0 object, L1157 mm (d=250 pc), reporting a deuterated molecule as a shock tracer for the first time.

The strong outflow activity and winds that YSOs produce result in high velocity gas, but also the evacuation of regions near the protostar. Such cavities have been previously seen as a ”hole” in the continuum emission (e.g. near NGC 1333 IRAS4 and SVS13; Lefloch et al. 1998). UV radiation from the protostellar system (mainly due to accretion) and/or related to shocks is expected to play a crucial role in such environments since it can penetrate over longer distances (Stäuber et al. 2004; Visser et al. 2012).

During the cold and dense pre-collapse phase, molecular complexity increases by rapid ion-molecule gas-phase reactions followed by gradual freeze-out and build up of ices (H_2O, CO, NH_3) and surface processes. While collapsing, the radiation that comes from the forming protostar heats the inner parts of the envelope making surface radicals mobile and highly reactive. Later, these freshly formed complex ices thermally desorb, further boosting rich chemical processes in the gas and creating a “hot corino” (e.g. Ceccarelli 2004, 2008). The hot corinos refer to inner regions (<200 au) with an increase of the temperature above 100 K, as a result of passive heating from the protostar.

In this work we are interested in answering the following questions: What is the chemical structure of low mass protostellar envelopes and how does it compare to high mass protostellar envelopes? How do the outflows influence the chemistry of the surroundings of a protostar?

For this purpose we use the low mass protostar IRAS 4A which appears as the brightest continuum object in NGC 1333 IRAS 4 region and is classified as Class 0 object (André et al. 1993). IRAS 4A is a prototype well studied Class 0 object and of great interest as it is among the first (Mathieu 1994), and youngest (André et al. 1993) protobinary systems ever detected. NGC 1333 is one of the nearest (D=235 pc; Hirota et al. 2008) and youngest ($<$ 1 My; Gutermuth et al. 2008) star forming regions. IRAS 4A is

actually a binary system, consisting of two deeply embedded Class 0 YSOs with a separation of 1.″8 (420 au at a distance of 235 pc). The binary nature of IRAS 4A had first been observed in 0.84 mm CSO–JCMT interferometric high–resolution submillimeter continuum observations (Lay et al. 1995) and resolved at millimeter wavelengths using the BIMA array by Looney et al. (2000b). They were also found to share a common circumbinary envelope (Looney et al. 2003).

In addition, a spectral line and continuum survey using SMA was performed by Jørgensen et al. (2007) where inverse P–Cygni ^{13}CO 2–1 (low–density) line profiles have been found. These profiles indicate infall motions, which are also a characteristic of Class 0 stage. Di Francesco et al. (2001b) reported inverse P–Cygni profiles in CS and H_2CO, tracing high–density gas and observed by IRAM Plateau de Bure.

IRAS 4A has been suggested to have a "hot corino" (Maret et al. 2004b). Multitransition observations of species such as H_2CO and CH_3OH towards 4A revealed abundance enhancement in the inner warmest regions (>100 K) by up to 2 orders of magnitude (Maret et al. 2004b, 2005). The same abundance enhancement can also occur in outflows on larger scales as a result of ice mantle sputtering in shocks (Bachiller & Pérez Gutiérrez 1997; Tafalla et al. 2000). Mantle sputtering is thought to play a role when outflow speeds reach about 10 km s^{-1} and is independent of gas density. In shocks with speeds as high as 20–25 km s^{-1} the mantles vaporize completely. As an example, H_2CO and CH_3OH have been found to trace outflow activity of IRAS 4A, which make it difficult to distinguish between a "hot corino" chemistry and the enhancement due to shocks caused by the protostellar outflows.

The highly collimated outflows from IRAS 4A have been mapped in several CO transitions (Yıldız et al. 2012; Jørgensen et al. 2007; Knee & Sandell 2000). IRAS 4A shows two bipolar outflows, one with a N–S orientation and the other with P.A. $\sim$45°, likely due to the binary nature of the system. The extended spatial distribution of the outflows in combination with broad lines towards 4A (i.e. large range of velocities) suggests that the inclination of the second outflow is $< 45°$.

In this article we present HIFI and JCMT observations of a range of chemically diverse species towards IRAS 4A. We first estimate the excitation temperature and column density of H_2CO in the envelope and outflow using population diagrams. We proceed with modeling our observed maps with RADEX in order to determine the DCO^+/HCO^+ and test the enhancement observed by Fontani et al. (2014a). Then, we apply the 1D physical model determined by Kristensen et al. (2012b) that takes into account the temperature and density gradients of the envelope and we run RATRAN in order to fit our observations. We apply constant and enhanced abundance profiles. In addition, we run chemical models that similarly take into account the physical structure of the protostellar envelope and apply the abundance profiles we determine to our RATRAN models and we compare those results with the empirical models.

We compare this low–mass case with the high–mass case of AFGL 2591 for which a similar analysis was performed by Kaźmierczak-Barthel et al. (2015). Lastly, we try to constrain the chemical age of the IRAS 4A from our time-dependent chemical models.

5.2 Observations and data reduction

5.2.1 HIFI: observations and reduction

Observations of the YSO NGC 1333 IRAS 4A (RA=$03^h29^m10.3^s$, Dec=$+31^o13'31''$ [J2000]) were made with the HIFI instrument on board of the Herschel Space Observatory, as a part of the CHESS guaranteed time key programme (Chemical Herschel Survey of Star Forming Regions; Ceccarelli et al. 2010). Full spectral scans were made in bands 2a and 2b, covering the spectral ranges 626.01–721.48 GHz (415.81–479.23 μm) and 714.02–800.90 GHz (374.58–420.16 μm), respectively, at a resolution of 1.1 MHz (0.41–0.53 km s^{-1}). In this frequency range, the Herschel/HIFI Half Power Beam Width (HPBW) is 26.5–33.9″ (Roelfsema et al. 2012). The spectral scan was performed in Dual Beam Switch (DBS) mode with a normal chop frequency of 0.17 Hz. Each sky frequency was covered four times to facilitate the double sideband deconvolution process. The instrument stability settings were calculated in HSPOT by fixing the minimum and maximum goal resolutions to 1.1 MHz and setting the 1 GHz reference option without continuum optimization.

The observations were processed with the pipeline at the Herschel Science Center with HIPE 7.1.0 and retrieved from the Herschel Science Archive. Further post–pipeline level 2 processing was done in HIPE 8.0. Since we are interested in full spectral coverage, only the WBS spectra were considered, although many HRS spectra in narrower range were also available. Spectral regions affected by 'spurs' and not automatically detected by the HIFI pipeline were flagged out and ignored. Polynomial baselines were subtracted using the FitBaseline task by masking the lines interactively. The overlapping sidebands were deconvolved with the doDeconvolution task in HIPE by applying the default settings. The observed line intensities in units of antenna temperatures were corrected for loss in the sidelobes by converting them to main beam temperatures using the main beam efficiency of η_{mb} (Beff/Feff) of 0.75 (Roelfsema et al. 2012).

5.2.2 JCMT: observations and reduction

These observations are a part of the JCMT Spectral Legacy Survey (SLS; Plume et al. 2007). The Auto–Correlation Spectral Imaging System (ACSIS) was used at the James Clerk Maxwell Telescope (JCMT[1]) on Mauna Kea, Hawaii.

We have $2' \times 2'$ maps from HARP–B instrument which provides high velocity resolution (1 MHz, $\sim$ 1 km s^{-1}). These observations cover the frequency window between 330 and 373 GHz. The angular resolution of JCMT is $\sim 15''$ at 345 GHz which is equivalent to $\sim$ 3500 au at the distance of NGC 1333 IRAS 4 (Choi et al. 2004). The beam efficiency is 0.63 (Buckle et al. 2009).

[1]The James Clerk Maxwell Telescope is operated by the Joint Astronomy Centre on behalf of the Science and Technology Facilities Council of the United Kingdom, the Netherlands Organization for Scientific Research, and the National Research Council of Canada.

Details regarding the reduction and line detections of this dataset can be found in Koumpia et al. (submitted).

5.3 Observational results

5.3.1 Line detections

The Single Side Band (SSB) H and V–polarization HIFI spectra were searched independently for line detections. We consider as safe detections the signals that were detected in both polarizations, were $> 3\times$RMS (RMS $\sim$ 0.01 K–0.04 K) after averaging, and which were characterised by a width of at least two channels > 0.9 km s^{-1} (single channel; 1.1 MHz, $\sim$0.47 km s^{-1}). Table 5.6 presents the line list with secure detections. The detected lines were identified by producing single temperature LTE models in CASSIS[2] of the species detected in SLS by Koumpia et al. (submitted). The species that are identified following this process are: CO, ^{13}CO, C^{18}O, CS, HCN, HCO$^+$, N_2H^+, H_2CO, CH_3OH, H_2S and H_2O. We inspected our HIFI spectra for lines of SO, SO_2, SiO, HNC, and H_2O isotopologues, but without detections.

The JCMT observations have been described in more detail in Koumpia et al (submitted), where the detected species towards IRAS 4A are also presented. In addition to the species detected in the HIFI survey, we detect the deuterated species DCO$^+$, HDCO, D_2CO, the S–bearing species SO, SO_2 and finally SiO, HNC, CN, C_2H, OCS. The overall rms noise level in the JCMT data ranges between 0.005 and 0.05 K at the velocity resolution of 0.9 km s^{-1}.

5.3.2 Line profiles

Examples of line profiles from species detected with HIFI and JCMT are plotted in Figures 5.1–5.3. Large line profile variations are observed. The CO 6–5 line shows narrow emission (FWHM$\sim$0.8 km s^{-1}) and absorption peaks accompanied by prominent wings extending over 25 km s^{-1} toward blue and red–shifted velocities. The absorption is absent in the other CO isotopologues, and the wings are much weaker. On the other hand, the H_2O line shows only very broad emission, very similar to the CO 6–5 wings (Figure 5.1).

Visually, the detected lines can be divided in 3 groups. These groups are characterized by line profiles that are dominated by a) broad emission (FWHM=4–11 km s^{-1}; Figure 5.2) such as CS, H_2O, HCN, CH_3OH and H_2CO, b) narrow emission (FWHM$<$4 km s^{-1} such as C^{18}O, ^{13}CO, H_2S, HCO$^+$ and N_2H^+ (Figure 5.3), and c) showing absorption features such as CO 6-5 and H_2S 2_{12}–1_{01} (Figure 5.1). To quantify the difference between the line profiles, they were decomposed with a simultaneous fit of three Gaussians: broad emission, narrow emission, and narrow absorption components (Table 5.6).

Our observations show that there is considerable variation in the width of the broad emission line components. With median FWHM values of 4.6 and 5.1 km s^{-1}, the H_2CO

[2]CASSIS has been developed by IRAP-UPS/CNRS (http://cassis.irap.omp.eu)

and CH_3OH lines are narrower than the H_2O line (11 km s^{-1}).

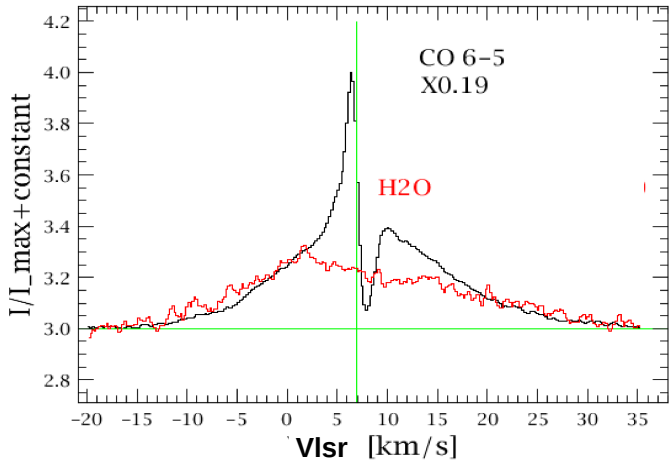

Figure 5.1: Normalized line profiles of H_2O 2_{11}–2_{02} (red) and CO 6–5 (black) scaled by 0.19 for easier comparison. The H_2O profile is very similar to the CO broad wing emission. The vertical green line represents the central velocity of the source at 6.7 kms^{-1}.

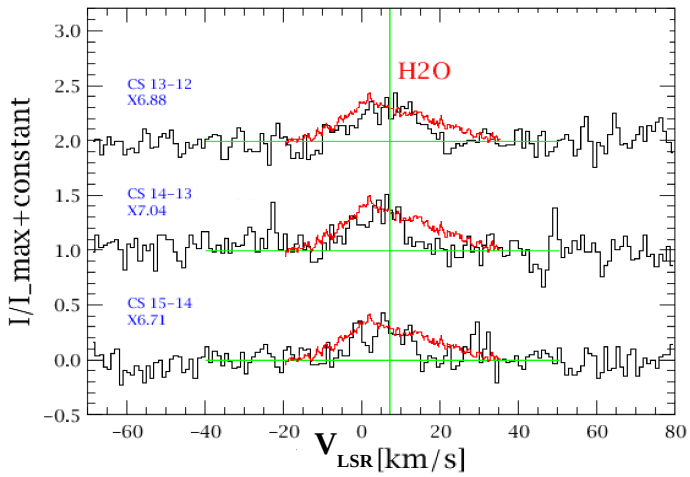

Figure 5.2: Same as Figure 5.1 but for CS line profiles (black).

The H_2O line itself is in fact asymmetric, and can be fitted with an additional, narrower Gaussian (V_{LSR} = 0.55 km s^{-1}, FWHM=3.86 km s^{-1}). Finally, it is worth mentioning that the peak positions of the narrow N_2H^+ lines are shifted by +0.6 km s^{-1} compared to H_2S and the CO isotopologues, similar to the absorption component seen in CO 6–5 and H_2S. The existence of such variation in the shape of the lines can be a result of the different regions that these lines trace. A broad component is indicative of outflow activity, a narrow component arises from dynamically quiescent gas (i.e. envelope) and the absorption is a result of infall motions or the presence of foreground material.

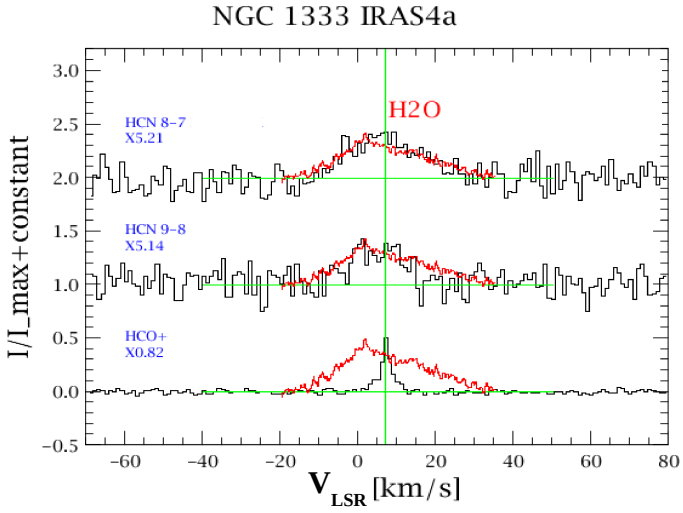

Figure 5.3: Same as Figure 5.1 but for HCN and HCO^+ (black). The shape of the HCN line profile is comparable to the H_2O but HCO^+ is narrower.

5.4 Physical conditions

5.4.1 LTE column densities

The protostellar envelope of NGC 1333 IRAS 4A has been previously studied by various authors (e.g. Maret et al. 2004b, 2005), a fact that does not apply for its associated outflow. In this section we aim to estimate the column density and excitation temperature from the observed emission in the envelope and outflow of IRAS 4A and compare their derived conditions. In our approach we also add the observed HIFI transitions that were not available in previous studies.

A widely used and simplified method for a rough estimation of the column density of a molecule is a population diagram (Goldsmith & Langer 1999) under the assumption of LTE. When LTE applies the T_{ex} equals the gas kinetic temperature, otherwise it provides only a lower limit.

The column density of the upper state N_u and the rotational temperature T_{rot} (=T_{ex}) once in LTE can then be determined by:

$$\frac{N_u}{g_u} = x\frac{\int T_{mb}dV}{\nu\mu^2 S} = \frac{N_T}{Q(T_{rot})}e^{-\frac{E_u}{T_{rot}}} \tag{5.1}$$

where x = 8.591×10^{37} $8\pi k/hc^3$, N_u the column density of the upper energy level (cm^{-2}), g_u the degeneracy of the upper energy level, T_{mb} the main beam temperature (K), dV the velocity range (km s^{-1}), ν the frequency (Hz), μ the dipole moment, S the line strength, N_T the total column density (cm^{-2}), T_{rot} the rotational temperature (K), Q the partition function and E_u the upper energy level. Plotting $\ln(N_u/g_u)$ versus E_u/k results in a straight line with a slope of $1/T_{rot}$.

In non-LTE excitation the population of each level may be characterized by a different excitation temperature T_{ex} ($\neq T_{rot}$). The population diagrams can also take into account optical depth and beam effects due to different angular resolutions among the lines by using the modified equation:

$$ln\frac{N_u}{g_u} = ln\frac{N_{T,thin}}{Q(T_{rot})} - \frac{E_u}{kT_{ex}} - ln(C_\tau) + ln(f) \tag{5.2}$$

where T_{ex} is the excitation temperature, $C_\tau = \tau/(1\text{-}e^{-\tau})$ is the optical depth correction factor, and f the beam dilution which is defined as the size of the telescope beam over the size of the emitting region which is assumed equal for all lines. A more detailed description of the method and formulas used can be found in Goldsmith & Langer (1999).

The velocity information of our lines allows us to fit multiple Gaussians and separate the outflow activity from the emission that comes from the dynamically quiescent envelope. For a more accurate determination of the temperature, species with sufficient amount of transitions are preferred. We perform this analysis for H_2CO for which we have observed many transitions with JCMT and HIFI (12). In this approach we include also 4 extra transitions as observed using IRAM and presented in Maret et al. (2004b).

Figures 5.4 and 5.5 present the population diagrams for the envelope and the outflow respectively, and the resulting excitation temperature, column density, optical depth and size of the emitting area. We find $T_{ex} \sim 35\pm0.5$ K and N(H_2CO) of $8.5^{+1.2}_{-0.8}\times10^{14}cm^{-2}$ for the envelope and $T_{ex} \sim 41.5\pm4$ K and N(H_2CO) of $1.2^{+0.5}_{-0.2}\times10^{15}cm^{-2}$ for the outflow. The error estimates have been computed during the χ^2 minimization procedure for $\Delta\chi^2=1$. Maret et al. (2004b) modeled only the envelope and found a factor of 2 lower column density and a factor of 1.2 lower T_{ex}. We attribute these differences to the use of the HIFI transitions which probe denser/warmer regions.

The excitation temperature provides only a lower limit for the gas kinetic temperature when the source is not in LTE. Our results point towards 2.5 times lower T_{ex} and 3 times

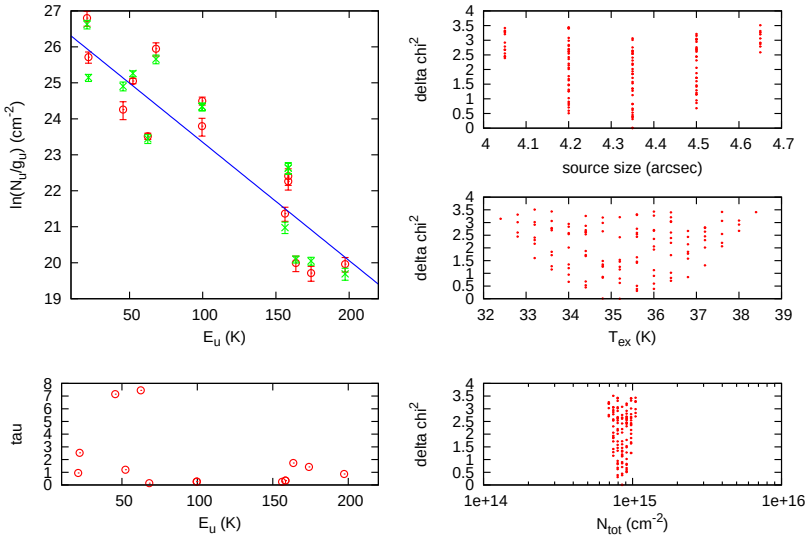

Figure 5.4: Results of population diagram based on the narrow component (envelope) of H_2CO as observed with JCMT and HIFI and the additional IRAM transitions as taken by Maret et al. (2004b). The plot presents the resulting excitation temperature, column density, optical depth and size of the emitting area. The red symbols represent the observed data, the green symbols represent the best fitted data, and the blue line represent the rotation diagram fit.

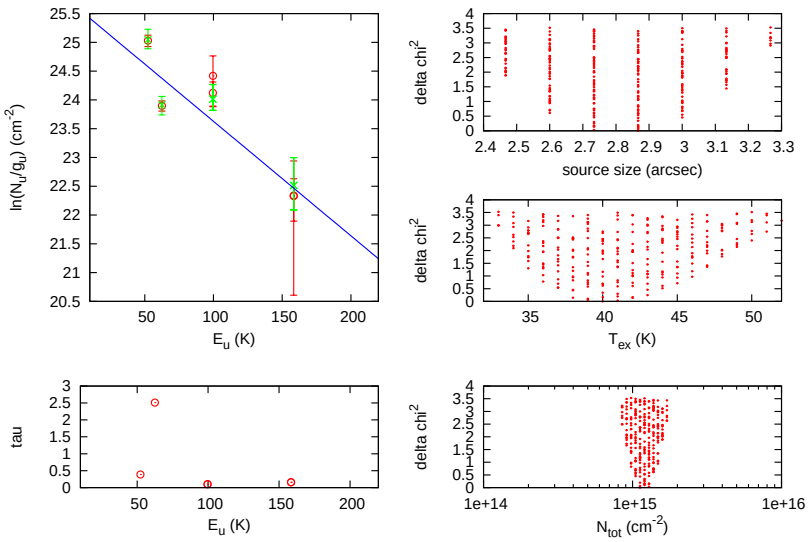

Figure 5.5: Same as in Figure 5.4 but for the broad component (outflow) of H_2CO. The H_2CO transitions observed with HIFI were fitted by a single component and are not included in this plot.

higher H_2CO column density for the envelope compared to the outflow. The fact that we can have a reasonable fit for both components using both resulting values though indicates that the observed difference is not significant.

5.4.2 Deuterated species and outflows

Pre-stellar cores have been characterized as "deuterium fractionation factories" (Ceccarelli et al. 2014), due to the high deuteration that has been observed towards them in various studies (>10% Bacmann et al. 2003; Crapsi et al. 2005b).

More recently, deuterated species have been employed as shock tracers by Fontani et al. (2014a). They found an enhancement of HDCO/H_2CO (∼10%) towards the eastern wall of the cavity excavated by the shock associated with the Class 0 object, L1157 mm. This is at least an order of magnitude larger than the HDCO/H_2CO ratio of the surrounding material. We aim to study the distribution of the deuterated species in the region and examine the deuteration towards the outflow of NGC 1333 IRAS 4A, which is also a Class 0 object.

In search of ions and deuterated species towards the outflow

The outflow activity of IRAS 4A has been traced by many species. SiO is expected to be a tracer of outflow shocks, due to sputtering of Si off dust grains (Schilke et al. 1997). Choi (2005) found it to trace the jet in the case of NGC 1333 IRAS 4. They have presented a map of SiO 1–0 which traces the outflow activity of IRAS 4A and the spatial distribution of a narrow line component offset at ∼7.6 km s^{-1}. Our dataset shows that the SiO 8–7 has its primary peak at the shock position north of IRAS 4A (R1; Santangelo et al. 2014), while SO also emits significantly at that position (Figure 5.6). The same figure shows the integrated intensity map of C_2H (core; from +5 to +9 km s^{-1}) which was found to trace the envelopes of the three ptotostars. Its three peaks are in alignment with the continuum peaks as observed by Sandell & Knee (2001).

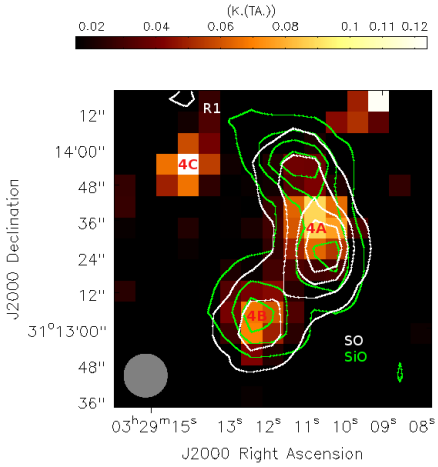

Figure 5.6: C_2H map overplotted with SiO in green contours (0.013, 0.03, 0.04, and 0.05 K; rms∼0.005 K) and SO in white contours (0.07, 0.02, 0.03 and 0.04 K; rms∼0.005 K).

Figures 5.7 and 5.8 present the spatial distribution of the observed deuterated species D_2CO, HDCO, DCO^+ and H_2D^+ as overplotted with C_2H. HDCO and D_2CO trace mainly the protostellar envelopes and their distribution covers part of the outflow-shock area (white rectangle) north–northeast of IRAS 4A (R1; Santangelo et al. 2014). DCO^+ traces the envelopes but it also emits in a more extended area between the sources in the NW–SE direction. Interestingly, H_2D^+ shows a very different spatial distribution compared to the other deuterated species. It does not follow the distribution of the envelopes and it mainly emits in the NW–SE direction in the space between the three sources. The spatial distribution of o-H_2D^+ as presented in Figure 5.8 appears to be co–spatial with the narrow component of SiO as presented by Choi (2005).

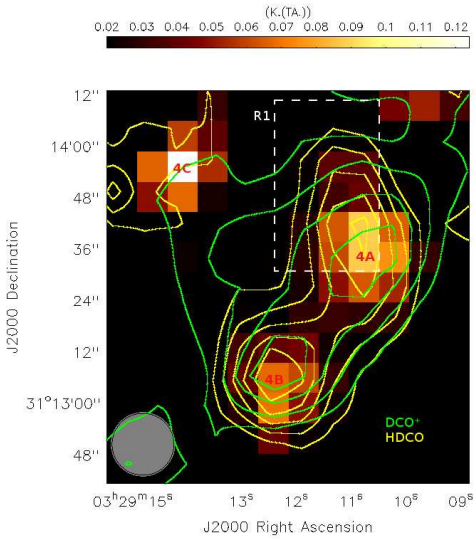

Figure 5.7: C_2H map overplotted with DCO^+ in green contours (0.04, 0.06, 0.09, and 0.15 K; rms∼0.005 K) and HDCO in yellow contours (0.013, 0.024, 0.034, 0.045 and 0.06 K; rms∼0.005 K).

Origin of o-H_2D^+ emission

H_2D^+ is expected to arise from very cold gas where CO is depleted. At very low temperatures (<20 K) the reaction $H_3^+ + HD \longleftrightarrow H_2D^+ + H_2 + \Delta E$ is not balanced by the backward process, increasing the abundance of H_2D^+. In addition the freeze out of CO and N_2 that would normally destroy H_2D^+ (e.g. Bacmann et al. 2003; Caselli et al. 2003, 2008), results in an increases of H_2D^+ abundance.

Given the "special" spatial distribution of H_2D^+, the logical follow-up is to investigate the spatial distribution of HCO^+ and N_2H^+. HCO^+ and N_2H^+ are produced through the reactions: $H_3^+ + CO \Longrightarrow HCO^+ + H_2$ and $H_3^+ + N_2 \Longrightarrow N_2H^+ + H_2$. In dense and very cold environments both CO and N_2 are expected to be depleted and thus so do HCO^+

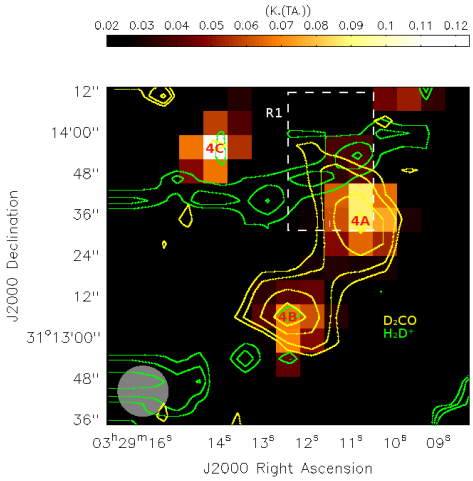

Figure 5.8: The spatial distribution of deuterated species in IRAS 4 region. Integrated intensity map (core; from +5 to +9 km s^{-1}) of C_2H which traces the envelope in colors, overplotted with H_2D^+ in green contours and D_2CO in yellow contours. The contour levels are set to 0.014, 0.016, 0.023 and 0.03 K (rms∼0.005 K).

and N_2H^+. Previous observations of N-bearing species (e.g. N_2H^+) towards prestellar cores have shown depletion resistance compared to CO, and that N_2 depletes at later times compared to CO (Bergin & Tafalla 2007b; Pagani et al. 2012). This contradicts the expectation of similar behavior in terms of freezing out and desorption mechanisms, since both species have similar masses and dipole moments.

Figure 5.9 presents the integrated intensity map of HCO^+ overplotted with H_2D^+ and N_2H^+ in contours. This figure shows that N_2H^+ and HCO^+ follow similar spatial distribution, tracing mostly the protostellar envelopes and they emit significantly in almost the half of the H_2D^+ slab towards the N–NW axis.

The presence of N_2H^+ and HCO^+ in part of the H_2D^+ slab can be a result of the outflow–shock activity in the region that volatile ices such as CO and N_2. If we assume a single layer of gas, such activity should also make H_2D^+ less abundant, but this is not what we observe. Previous studies including Choi et al. (2004) and Koumpia et al (submitted) provided evidence for a foreground cloud at ∼8 km s^{-1} and IRAS 4A and IRAS 4B are a part of a smaller embedded cloud at 6.7 km s^{-1}. The H_2D^+ line is shifted by ∼1.5 km s^{-1}. This can be an indication that the narrow component of SiO 1–0 (∼7.6 km s^{-1}) and the H_2D^+ (∼8 km s^{-1}) originate from the same foreground layer at the offset velocity. Such narrow SiO emission has been discovered in more regions (e.g. G035.39–00.33) and it has been suggested that it originates from cold gas associated with a low-velocity shock (e.g. Duarte-Cabral et al. 2014b). H_2D^+ emission requires very cold conditions though and is unlikely to be associated with shock activity due to the presence of N_2H^+ and HCO^+. This emission probably originates from a colder layer

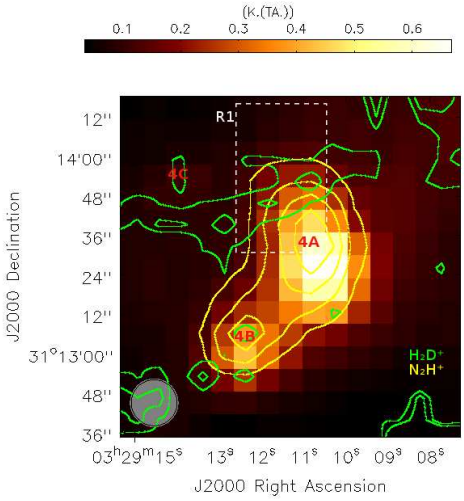

Figure 5.9: HCO^+ integrated intensity map overplotted with H_2D^+ in green contours (0.017, 0.026 K; rms$\sim$0.005 K) and N_2H^+ in yellow contours (0.14, 0.27, 0.41 and 0.54 K; rms$\sim$0.005 K).

in the foreground.

Modeling the deuteration

In order to model the observed emission and determine the deuteration of the region we use the kinetic temperature map as derived by Koumpia et al. (submitted) in the non–LTE radiative transfer program RADEX (van der Tak et al. 2007b) after adopting a constant H_2 density of 3×10^5 cm^{-3} as suggested in the same work. We calculate and present the [DCO^+]/[HCO^+] ratio in Figure 5.10. Because of the adopted constant density the absolute values of the resulting column densities can vary by up to a factor of 3. Assuming that the gas surrounding the protostars is characterized by densities $< 3\times10^5$ cm^{-3} would cause a decrease in the resulting kinetic temperature by a factor up to $\sim$2 and an increase in the resulting column densities by a factor up to $\sim$3. The uncertainties of this method are based on the best fit models (χ^2 minimization) after keeping 1 fixed parameter per run (described in detail in Koumpia et al.; submitted).

We find $\sim$3 times higher [DCO^+]/[HCO^+] ratio towards the N–NE part of the H_2D^+ slab compared to the sources while the N–NW part of the slab does not show an enrichment in deuteration. The shock position on the north though (R1) is characterized by values equal and up to 2 times higher deuteration compared to IRAS 4A.

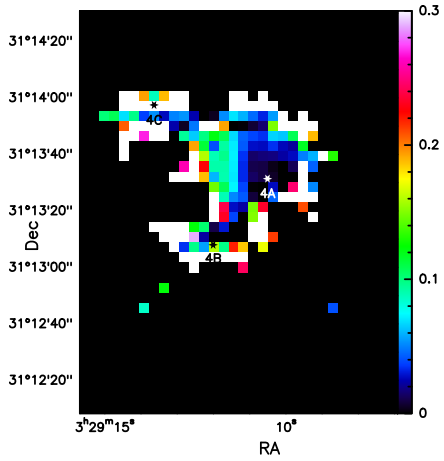

Figure 5.10: Spatial distribution of the modeled [DCO^+]/[HCO^+] ratio.

5.5 Chemical structure of the envelope

5.5.1 RATRAN – model setup

In order to estimate molecular abundance profiles through the envelope of NGC 1333 IRAS 4A, we ran the Monte Carlo radiative transfer code RATRAN (Hogerheijde & van der Tak 2000) and produced synthetic line emission. RATRAN takes into account the physical structure of the source including temperature and density gradients, and continuum dust emission and absorption.

The line spectra of NGC 1333 IRAS 4A are generally broad (>5 km s^{-1}) and the wings are very prominent in many species. The physical models are determined using continuum observations that characterize the protostellar envelope. Therefore we focus on the narrow component of the lines. For this purpose we perform a multi-Gaussian fit and use only the narrow component for modeling. Some of the lines show self–absorption making the accurate Gaussian fitting very difficult and the modeling of the lines more complicated. Thus, we chose not to work with those lines.

The H_2O line shows only a broad component (Figure 5.1) and we observe no isotopologues, making the identification of the envelope component unreliable. The situation for SiO is similar, thus we do not model these species. We model the isotopologues preferably when present, and otherwise model the narrow component of the main species when multiple Gaussian fitting is possible (e.g. $H^{13}CO^+$, $C^{17}O$ and $C^{18}O$, $H^{13}CN$). We use fixed local ISM isotopic ratios of $^{12}C/^{13}C = 60$, $^{16}O/^{17}O = 2000$, $^{16}O/^{18}O = 560$ (Wannier 1980; Wilson & Rood 1994; Wilson 1999). In addition we assume an ortho to para ratio of 3 for the two collisional partners o–H_2 and p–H_2. Dust continuum radiation is taken into account using the dust opacity OH5 taken from Ossenkopf & Henning (1994b) (Table 1), which corresponds to dust grains with thin ice mantles.

We ran RATRAN applying the density and temperature radial profiles of NGC 1333 IRAS 4A

(Figure 5.11) as determined by Kristensen et al. (2012b). The density profile is assumed to be a power–law, $n(r) = n_0 \times (r/r_0)^{-p}$, with a best–fit index of $p = 1.8$. The density and temperature profiles were derived from the best–fit dust model assuming that the gas is entirely molecular and using a mean molecular mass of 2.4 amu and a gas–to–dust ratio of 100. For our calculations we defined a grid of 19 spherical shells from $r_{in} = 5\times10^{14}$ cm up to $r_{out} = 7.7\times10^{16}$ cm where the dust temperature is 250 K and 10 K and the n_{H_2} density is 3.05×10^{9}cm^{-3} and 3.5×10^{5}cm^{-3} respectively. The original model extends further out as seen in Figure 5.11 but our adopted profiles better represent the size and outer temperature of the envelope of a protostar ($\sim$5000 au, 10 K). We also assumed thermal equilibrium between dust and gas at those high densities.

The papers from which the collisional rate coefficients of the main isotopologues with H_2 were adopted, are presented in Table 5.1. The collisional data of H_2S are scaled from the files of ortho- and para-H_2O by ortho- and para-H_2 as calculated by Dubernet et al. (2009); Daniel et al. (2010, 2011). For isotopologues and the deuterated species the same collision data were used as for the main isotope.

Table 5.1: References for the collisional rate coefficients of the species modeled in this paper.

Species	Authors
CO	Yang et al. (2010)
HCO^+	Flower (1999)
N_2H^+	Flower (1999)
HCN	Dumouchel et al. (2010)
CS	Lique et al. (2006); Lique & Kłos (2011)
HNC	Dumouchel et al. (2010)
H_2CO	Wiesenfeld & Faure (2013)
CH_3OH	Rabli & Flower (2010)
C_2H	Müller et al. (2005)
CN	Lique et al. (2006); Lique & Kłos (2011)
OCS	Green & Chapman (1978)
SO_2	Green (1995)
H_2CS	Wiesenfeld & Faure (2013)

We assumed a static envelope without infall or expansion and we used a range of abundances typically varying between 10^{-7} and 10^{-12} in order to constrain the abundance profile that best fit the observations. The turbulent line width was fixed to 1.9 km s^{-1}, which is the average value we found for the narrow component of most species after fitting multiple Gaussians. Modeling the observed lines with a constant abundance is the only way when it comes to species which show only a few transitions but might be not always a realistic approach. Several molecules have been suggested to be present in volatile ice mantles on dust grain surfaces at temperatures $<$ 20–110 K. The exact temperature depends on species and the surface composition (Bisschop et al. 2006; Herbst & van Dishoeck 2009). We chose to apply jump–like abundances at 100 K for H_2CO and

Table 5.2: Constant empirical abundances estimated with RATRAN for the envelope of NGC 1333 IRAS 4A based on HIFI and JCMT observations. The table contains also the abundances of AFGL 2591 (outer envelope) for direct comparison.

Molecule	Abundance	
	IRAS 4A	AFGL 2591 (outer)
CO	3×10^{-5}	2×10^{-4}
HCO^+	1×10^{-9}	3×10^{-8}
N_2H^+	8×10^{-11}	8×10^{-10}
HCN	3×10^{-10}	5×10^{-7}
CS	3×10^{-9}	4×10^{-8}
HNC	8×10^{-11}	1×10^{-8}
H_2CO	4×10^{-10}	1×10^{-8}
CH_3OH	1×10^{-8}	8×10^{-8}
DCO^+	1×10^{-11}	...
C_2H	6×10^{-10}	8×10^{-8}
CN	1×10^{-10}	1×10^{-9}
OCS	6×10^{-9}	4×10^{-8}
SO_2	4×10^{-10}	5×10^{-9}
HDCO	5×10^{-11}	...
H_2CS	4×10^{-10}	4×10^{-9}
D_2CO	5×10^{-11}	...
H_2S	4×10^{-10}	4×10^{-9}

Table 5.3: As Table 5.2, but for jump and drop abundance profiles.

	IRAS 4A		AFGL 2591		Jump/
Molecule	X_{IN}	X_{OUT}	X_{IN}	X_{OUT}	Drop at
CO	1×10^{-4}	3×10^{-6}	2×10^{-4}	(const.)	25 K
H_2CO	4×10^{-8}	4×10^{-10}	1×10^{-11}	1×10^{-8}	100 K
CH_3OH	1×10^{-8}	7×10^{-10}	8×10^{-7}	8×10^{-8}	100 K

CH_3OH for which more transitions are available.

5.5.2 RATRAN – model results

The resulting abundances from the process described above are presented in Table 5.2 which compares this low mass case with a high mass case from the literature (AFGL 2591; Kaźmierczak-Barthel et al. 2015). We find observed abundance profiles for the low mass protostellar envelope (NGC 1333 IRAS 4A) which are systematically 1 to 2 orders of magnitude lower than the high mass protostellar envelope.

Figure 5.12 shows the observed line profiles of $C^{17}O$ 3-2 and $C^{18}O$ 6-5 with overplotted the best fit abundance profile model after deriving a constant abundance of 3×10^{-5} and a drop model for comparison. Using a constant abundance, it was impossible to re-

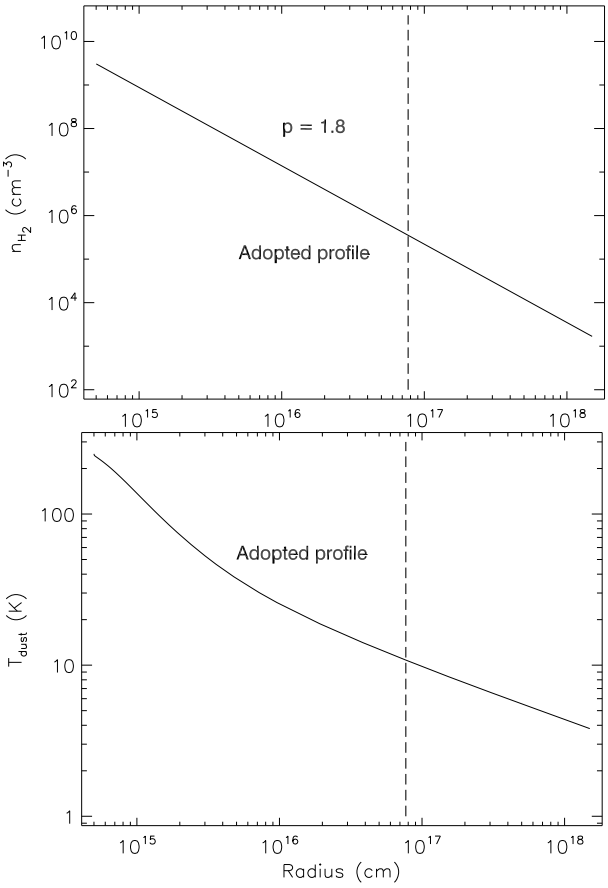

Figure 5.11: The density (top) and temperature (bottom) profiles of NGC 1333 IRAS 4A as derived by Kristensen et al. (2012b). The dashed line represents the outer radius adopted for our models (T$\sim$10 K).

produce the intensities of both $C^{17}O$ and $C^{18}O$ lines with this profile. Taking into account the freeze–out zone one would expect a drop of the CO abundance but this alone is also not able to reproduce the line intensities. Thus, we use a similar drop profile as suggested by Yıldız et al. (2010, 2012), in which the abundance of CO drops in the freeze–out zone but rises again in the outer envelope. The evaporation temperature of CO is not well-determined, so we chose to use the lower limit from laboratory, which is 25 K. We find the best fit model is one that adopts an inner abundance for T>25 K of 1×10^{-4} which drops to 3×10^{-6} at the coldest part of the envelope and rises again to the canonical value of 1×10^{-4} towards the outer envelope where external UV radiation becomes important. This is in good agreement with the additional $C^{18}O$ transitions from Yıldız et al. (2012) who found a CO abundance of 6×10^{-5} for the warmest part of (250–50 K) the envelope dropping to 3×10^{-6} for the coldest part (<30 K) where depletion is prominent and a jump up to 3×10^{-4} for the outer envelope. The constant CO abundance reproduces the $C^{18}O$ 6–5 transition very well, but it overproduces by a factor of $\sim$2 the $C^{17}O$ 3-2. Having additional transitions would help to better constrain the abundance profile. The fact that the higher–J $C^{18}O$ 6–5 can be reproduced by a constant abundance profile indicates that

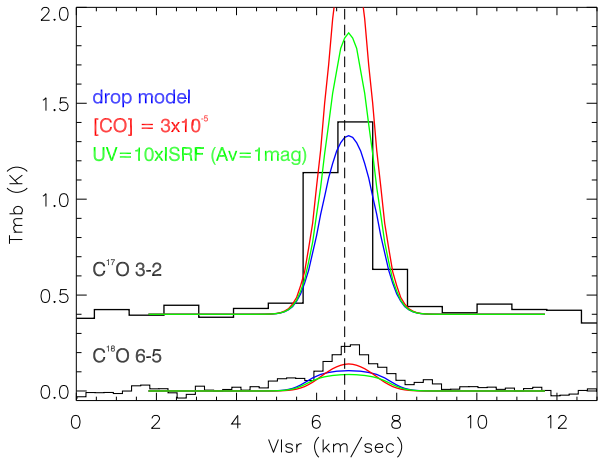

Figure 5.12: Observed $C^{17}O$ 3-2 and $C^{18}O$ 6-5 line profiles (black) overplotted with the modeled line profiles resulting in RATRAN after applying a) ∼1.5 orders of magnitude drop in CO abundance at the snowline (blue) b) CO constant abundance of 3×10^{-5} (red) and the abundance profile as adopted from our chemical models for UV=10×ISRF at A_V=1mag (black line in Figure 5.17).

CO evaporate back into the gas phase in the inner envelope (T >30 K). We chose to work with these isotopologues because they are optically thin and have narrow line-widths and thus trace the quiescent envelope. The fact that we avoiding using the optically thick broad ^{13}CO lines introduces less systematic errors in our solution.

Figure 5.13 shows the integrated intensities of the observed H_2CO transitions using HIFI and JCMT towards IRAS 4A overplotted with the convolved (∼15–33″) synthetic emission as calculated with RATRAN for a constant abundance of $[H_2CO] = 4\times10^{-10}$ and jump models at ∼100 K. The assumption of a constant abundance works well for the transitions with $E_{up} > 100$ K while the 2 transitions with $E_{up} < 100$ K are 15–50% overproduced, indicating that a jump model is required. Our jump model at ∼100 K results in $X_{IN} = 4\times10^{-8}$ and $X_{OUT} = 4\times10^{-10}$ and reproduces the lower energy lines better but the higher energy lines a bit worse compared to the constant abundance model. Maret et al. (2004b) found H_2CO abundance about a factor of 2 lower for the inner envelope (2×10^{-8}) and a factor of 2 lower for the outer envelope compared to our jump model. Differences up to 2 orders of magnitude between H_2CO abundance of the inner and outer low–mass protostellar envelopes have been observed before (IRAS 16293–2422; Ceccarelli et al. 2000).

Figure 5.13 shows the integrated intensities of the observed CH_3OH transitions using HIFI and JCMT towards IRAS 4A overplotted with the convolved (∼15–33″) synthetic emission as calculated with RATRAN for $[CH_3OH] = 1\times10^{-8}$. Maret et al. (2005) have found an upper limit of 1×10^{-8} for the CH_3OH abundance in the inner envelope and the same abundance as we do in the outer envelope. The main differences in the two methods are the additional HIFI transitions we use, the new collisional data and the new physical

model derived by Kristensen et al. (2012b) including PACS observations which were the smallest–scale used data. Maret et al. (2004b, 2005) used the physical model derived by Jørgensen et al. (2002). The models we used are characterized by the same power law for the density profiles and the temperature profiles also follow a similar pattern.

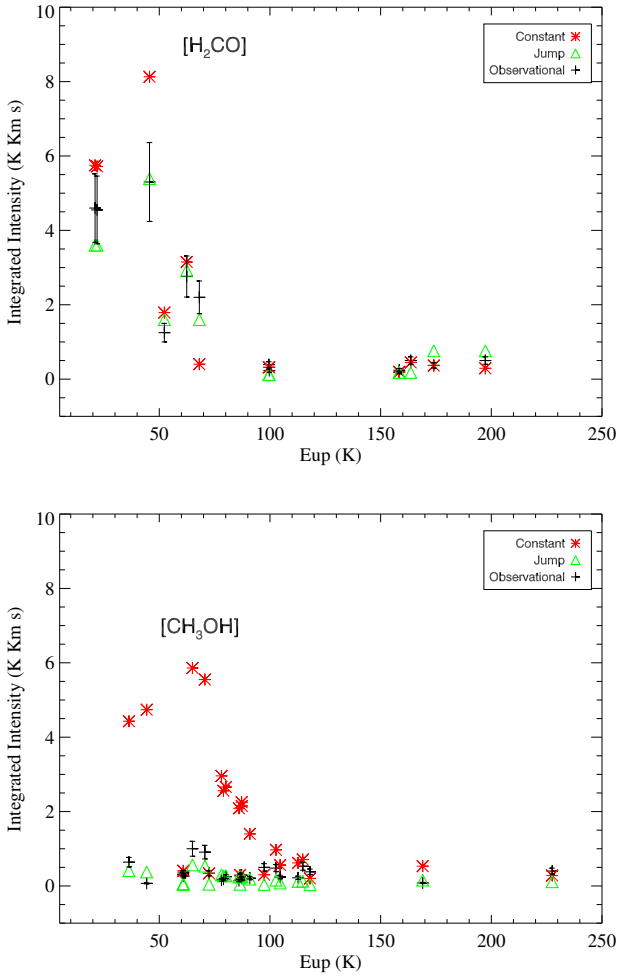

Figure 5.13: Integrated intensities of the observed (black) and modeled H_2CO and CH_3OH transitions in the observed E_{up} range using a constant abundance of [H_2CO] $= 4\times10^{-10}$ and [CH_3OH] $= 1\times10^{-8}$ (red) and a jump model (green). The errors of the observed values are $\sim$20% of the measured value.

We find HDCO/H_2CO ratio of $\sim$10% which is comparable with the one found by Loinard et al. (2000, 2001) towards IRAS 16293–2422 ($\sim$10–15%) and the value reported for Orion KL ($\sim$15%). We also find a very high D_2CO over H_2CO ratio ($\sim$10%) although this is based on only 1 transition. Very high values between $\sim$5–10% of the relative D_2CO abundance have been found before towards the low mass protostar IRAS 16293–2422 (Ceccarelli et al. 1998; Loinard et al. 2000), which is $\sim$2 orders of magnitude higher than in Orion KL. The average gas kinetic temperature of IRAS 4A is $\sim$45 K (Koumpia et al, submitted) and thus such high deuteration cannot be explained if D_2CO is only

formed in the gas–phase. On the other hand, D_2CO may have been enriched in the dust grains in low mass protostellar environments during the cold, dense pre–collapse period followed by its evaporation thus it is probably formed via the grain surface reactions. Lastly, we find $DCO^+/HCO^+ = 1\%$ in agreement with what is reported by Loinard et al. (2000, 2001) for IRAS 16293–2422.

5.6 Chemical modeling

5.6.1 Pseudo time-dependent model

In this section we compare the empirical abundance profiles of the studied species (RATRAN) with those resulting from chemical models for the same adopted physical structure of NGC 1333 IRAS 4A. Our goal is to a) understand the chemical processes that take place in NGC 1333 IRAS 4A and b) constrain its age.

To compare the observationally-derived abundance profiles, we used the same 1D physical model as in 5.5.1 and gas-grain time-dependent chemical model as in Kaźmierczak-Barthel et al. (2015). This allows us to compare chemistry modeling results between a low-mass and a high-mass protostellar envelope. The chemical model is based on the chemical kinetics ALCHEMIC code of Semenov et al. (2010) and a gas-surface network with deuterium fractionation (Albertsson et al. 2013, 2014). The original, non-deuterated chemical network stems from the osu.2007 ratefile developed by the group of Eric Herbst [3]. The network is supplied with a set of $\sim$ 1 000 high-temperature neutral-neutral reactions from Harada et al. (2010, 2012) and updated as of June 2013, using the KIDA database[4].

All H-bearing species reactions in this network were cloned by adding D, with the exception of molecules with the $-$OH functional group. Primal isotope exchange reactions for H_3^+ as well as CH_3^+ and $C_2H_2^+$ from Roberts & Millar (2000); Roberts et al. (2004); Roueff et al. (2005) were included. In cases where the position of the deuterium atom in a reactant or in a product was ambiguous, a statistical branching approach was used (for further details please consult Albertsson et al. 2013). In Albertsson et al. (2014) this deuterium network was further extended by adding ortho- and para-forms of H_2, H_2^+ and H_3^+ isotopologues and the related nuclear spin-state exchange processes.

To calculate ionization rates, we adopted the cosmic ray ionization rate of 5×10^{-17} s^{-1}, as derived by van der Tak & van Dishoeck (2000b) and Indriolo et al. (2015). In addition, we ran chemical simulations with a higher value of 10^{-16} s^{-1}. The photodissociation and photoionization rates in the model are adopted for a 1D slab model from van Dishoeck (2006). To mimic the presence of an outflow in this source, we also considered several other models with enhanced UV irradiation. For that, we use a scaled interstellar

[3] http://web.archive.org/web/20081204232936/
http://www.physics.ohio-state.edu/ eric/research_files/
osu_03_2008

[4] http://kida.obs.u-bordeaux1.fr

UV radiation field in Draine (1978) units and moderate dust extinction of 10, 3, 2, and 1 mag. The pre-computed photoionization and dissociation rates for a 1D plane-parallel slab model were used (see Eq. 5; Semenov et al. 2010). The self- and mutual-shielding of CO and H_2 from external dissociating radiation was calculated as in Semenov & Wiebe (2011). The water self-shielding is neglected.

The grains are uniform and spherical and made of amorphous olivine with a density of 3 g cm^{-3} and a radius of 0.1 μm. If grains are on average bigger than 0.1 μm it would slow down freeze-out which would increase the CO gas/ice ratio. The same effect would be seen for all other species that can freeze out. This would enhance the overall gas-phase molecular abundances with respect to our standard model. IRAS 4A is still a young object though, so no severe grain growth is expected.

Each grain provides $\approx 1.88 \times 10^6$ surface sites (Biham et al. 2001) for freeze-out of gaseous molecules. We use the desorption energies E_{des} from (Garrod & Herbst 2006). The binding energies E_b are computed by multiplying E_{des} by 0.4.

The gas-grain interactions include sticking of neutral species and electrons to dust grains with 100% probability and desorption of ices by thermal, cosmic ray, and UV-driven processes. In our model we use a single E_{des} for H_2 = 450 K, which properly describes H_2 diffusion over the dust surface and the H_2 binding to water or silicate surfaces. However, the H_2–H_2 binding energy is much lower (23 K). This means that as soon as there is a H_2 monolayer on a surface, further freeze-out of H_2 would be compensated by immediate desorption of H_2 back to the gas phase. Our models cannot capture this process well and thus we simulate it by not allowing H_2 isotopologues to stick to grains (See also; Hincelin et al. 2015).

The UV photodesorption yield of 10^{-3} was used (e.g., Öberg et al. 2009; Fayolle et al. 2011, 2013). This is consistent for CO and some other light species, but it drops to $\sim 10^{-5}$ or lower for anything bigger (e.g. CH_3OH). This is one of the limitations of our method. Photodissociation processes of solid species are taken from Garrod & Herbst (2006).

Surface recombination proceeds through the classical Langmuir-Hinshelwood mechanism (e.g. Hasegawa et al. 1992). The ratio between diffusion and desorption energies of surface reactants is taken to be 0.5 for all surface species. We do not allow tunneling of surface species via the potential wells of the adjacent surface sites. To account for hydrogen tunneling through barriers of surface reactions, we have employed Eq. (6) from Hasegawa et al. (1992), which describes a tunneling probability through a rectangular barrier with a thickness of 1 Å.

For each a surface recombination, we assume there is a 1% probability for the products to leave the grain due to the partial conversion of the reaction exothermicity into breaking the surface-adsorbate bond (Vasyunin & Herbst 2013). Following experimental studies on the formation of molecular hydrogen on amorphous dust grains by Katz et al. (1999), the standard rate equation approach to the surface chemistry is utilized. In addition, dissociative recombination and radiative neutralization of molecular ions on charged grains and grain re-charging are taken into account.

Table 5.4: Initial abundances for chemical modeling.

Species	Abundances
"Low metals" (LM), C/O = 0.44	
o-H_2	3.75×10^{-1}
p-H_2	1.25×10^{-1}
HD	1.55×10^{-5}
He	9.75×10^{-2}
C	7.86×10^{-5}
N	2.47×10^{-5}
O	1.80×10^{-4}
S	9.14×10^{-8}
Si	9.74×10^{-9}
Na	2.25×10^{-9}
Mg	1.09×10^{-8}
Fe	2.74×10^{-9}
P	2.16×10^{-10}
Cl	1.00×10^{-9}

With this network and 10^{-5} relative and 10^{-20} absolute tolerances, the 1D IRAS 4A model takes about 1 minute using Core-i7 2.5 GHz CPU (OS X 10.11, gfortran 6-x64) to compute over 10^6 years. This time span encompasses the likely age of this object.

5.6.2 Initial abundances

To set the initial abundances, we calculated the chemical evolution of a 0D molecular cloud with $n_{\rm H} = 2 \times 10^4$ cm^{-3}, T = 10 K, and $A_{\rm V} = 10$ mag over 1 Myr (model "PSC-LM"). For that, the neutral "low metals" (LM) elemental abundances of Graedel et al. (1982); Agúndez & Wakelam (2013) were used, with the solar C/O = 0.44, initial ortho/para H_2 of 3:1, hydrogen being fully in molecular form, and deuterium locked up in HD (see Table 5.5).

5.6.3 Error estimations

The problem of uncertainties of the calculated abundances is well known in chemical studies of various astrophysical environments, ranging from dark clouds and hot cores to protoplanetary disks and exoplanetary atmospheres (see, e.g., Dobrijevic et al. 2003; Vasyunin et al. 2004; Wakelam et al. 2005; Vasyunin et al. 2008). The error budget of the theoretical abundances is determined by both the uncertainties in physical conditions in the object and, to a larger degree, by uncertainties in the adopted reaction rate coefficients

Table 5.5: The top 25 of the initially abundant molecules for the NGC 1333 IRAS4A chemical modeling.

Species	Abundances
PSC-LM model with C/O = 0.44	
p-H_2	3.77×10^{-1}
o-H_2	1.23×10^{-1}
He	9.75×10^{-2}
H	5.25×10^{-4}
H_2O^*	5.53×10^{-5}
CO^*	4.05×10^{-5}
CO	3.26×10^{-5}
O_2	1.79×10^{-5}
HD	1.52×10^{-5}
N_2	7.39×10^{-6}
NH_3^*	5.64×10^{-6}
O	5.59×10^{-6}
O_2^*	4.12×10^{-6}
CH_4^*	3.64×10^{-6}
N_2^*	1.76×10^{-6}
H^*	6.03×10^{-7}
$C_3H_2^*$	4.48×10^{-7}
OH	3.43×10^{-7}
H_2O	2.79×10^{-7}
HNO^*	2.40×10^{-7}
NO	2.22×10^{-7}
N	1.36×10^{-7}
HDO^*	1.35×10^{-7}
CO_2	1.32×10^{-7}
CO_2^*	1.19×10^{-7}

* – denotes frozen species.

and their barriers. Poorly known initial conditions for chemistry may also play a role here.

In order to estimate the chemical uncertainties rigorously, one usually needs to perform a large-scale Monte Carlo modeling by varying reaction rates within their error bars and re-calculating chemical evolution of a given astrophysical environment. We do not attempt to perform such a detailed study and use the estimates from previous works.

In previous studies of chemical uncertainties it was found that the uncertainties are in general larger for bigger molecules as their evolution involves more reactions compared to simpler molecules. For simpler, key species such as CO and H_2 involved in a limited cycle of reactions it is easier to derive the reaction rates with a high accuracy of $\sim 25\%$. In addition these species are formed in the gas which is better known than the surface part. Consequently, their abundances are usually accurate within $10 - 30\%$ in modern astrochemical models. On the other hand, for other diatomic and triatomic species such as CN, HCO^+, HCN, CCH, etc. uncertainties are usually about a factor of 3-4 (see Vasyunin et al. 2008). The chemical uncertainties are even higher for more complex molecules like methanol due to the fact that gas phase reactions are less known and the surface chemistry less well understood. These uncertainties can reach orders of a magnitude, with the factor of 10 being a likely lower limit.

Moreover, for S-bearing species, for which many reaction rates have not been properly measured or calculated or included in the networks, these intrinsic uncertainties and hence the uncertainties in their resulting abundances are higher, $>$ factor of 10 even for simple species such as SO, OCS, and SO_2 (Loison et al. 2012). Also, the incompleteness of astrochemical networks with regard to the chemistry of Cl- and F-bearing molecules makes their calculated abundances rather unreliable.

In our study we assume that the uncertainties in the abundances of ortho- and para-H_2 and CO are within a factor of 30%. For HCO^+, H_2CO, CN, N_2H^+, C_2H, NO, OH, C, C^+, O, CH, NH_3, H_2O, HCN, HNC the uncertainties are within a factor of 3, and for S-bearing species, CH_3OH, and HCl they are within a factor of 10.

The result of this process is the abundance profiles from the species of interest. This means that we get the abundance of species over the radius adopted from the physical models for a range of timescales. In our study we do not use the abundance profiles of SO_2, SO, and OCS from the chemical model because the chemical network for S-bearing species is too inaccurate with respect to these species and thus lacks predictive power.

5.6.4 Results

Standard approach

Figures 5.14–5.16 present the results of the standard chemical modeling compared to the observed abundances of NGC 1333 IRAS 4A from Sec. 5.5.1 and the high mass protostellar envelope AFGL 2591 from Kaźmierczak-Barthel et al. (2015). The observed abundances for most species appear to be in agreement with the modeled abundances in the outer envelope while they are systematically 1 to 2 orders of magnitude lower than the high mass protostellar envelope. In contrast, the predicted CN, HCN, and HNC abundances are 1 to 2 orders of magnitude higher than the observed values for the outer envelope. Our chemical models do not take into account shielding of CN by H_2, as well as FUV scattering which can be important. In addition our models use the CN photodissociation rates which are taken by van Dishoeck et al. (2006). A more recent study by el-Qadi & Stancil (2013) presents CN cross sections with values several times

smaller than those from van Dishoeck et al. (2006). From all the parameters, it seems that the strongest effect in those modeled abundances is due to the assumed FUV intensity and the C/O ratio. The C/O = 1.1 gives X(CN) of 3×10^{-7} while X(HCN) $\sim$ X(HNC) $\sim 8\times10^{-10}$. If one assumes a strong FUV field of 10^4 of the ISF UV with a modest extinction of Av=1 mag, the fit is much better: X(CN) $\sim$1–4×10^{-10}, X(HCN) $\sim<10^{-11}$, X(HNC) $\sim> 2\times10^{-11}$. Without any additional FUV one gets X(CN) = 10^{-14}, X(HCN) $\sim 2\times10^{-9}$, X(HNC) $\sim 7\times10^{-11}$. The standard model alone cannot explain the observed abundances for more than one of the modeled species, making the development of a more advanced model necessary.

The necessity of an outflow cavity

We observe a drop of only $\sim$2 orders of magnitude towards the snowline of CO, compared to $\sim$6 orders of magnitude predicted by our chemical models. A plausible explanation for such a discrepancy between our chemical model and the observations is the presence of the outflow, which is not accounted for in the 1D model (Bruderer et al. 2009). The way to approximately simulate the outflow, the UV-irradiated outflow walls, and the envelope in the 1D approximation is to add more UV radiation to the chemical model. For that, additional FUV components with the intensities of 1 and 10 Draine and moderate dust extinction of 10 and 3 mag was considered. We find that only lower extinction influences the resulting CO abundance, increasing it by $\sim$1 order of magnitude. The standard model without extra UV radiation and an extinction of 10 mag produces the same abundance profiles.

Figures 5.17–5.19 present the results of the models with additional 10 Draine UV fields and for dust extinctions of 1, 2 and 3 mag. The extreme case of an 100 Draine UV field and A_V= 1 was also considered resulting in an almost constant CO abundance profile. Our observed CO abundance profile appears to be reproduced reasonably well by UV= 10$\times$ISRF and A_V= 1 mag (green line; Figure 5.12). Although such a model makes the overall fit better for CO, HCO^+ and DCO^+, it does not really improve the fit for other species (e.g. CS, CN, C_2H) and it actually makes overall fit worse for H_2CO, HDCO, D_2CO and CH_3OH, by decreasing the abundance of the outer envelope by up to 4 orders of magnitude. Thus, we do not consider it to be our best–fit (or standard) model.

The modeled HCO^+ abundances generally follow those of its parent molecule, CO, and show a strong decline for radii between $\sim 5\times10^{15}$ and 8×10^{16} cm, where the CO freezeout zone is located. HCO^+ abundances also drop strongly in the inner, dense and dark envelope region at r<2×10^{15} cm, where ionization degree drops due to fast recombination processes. Not surprisingly, the modeled N_2H^+ abundances also drop in the very inner envelope, like those of HCO^+. In contrast to HCO^+, N_2H^+ thrives in the CO freezeout zone, where a key destruction reaction of N_2H^+ ions by CO molecules is no longer effective. In Figures 5.15, 5.18 the DCO^+ abundances are compared, and the modeled DCO^+ profile follows the case of HCO^+ and agrees with observations in two areas: 1) inner envelope at $\sim 1-4\times10^{15}$ and 2) outer envelope with $r > 10^{17}$ cm.

In constrast to HCO^+, DCO^+ is slightly overproduced in the no-UV chemical model in the inner part of the envelope, but is well fitted by the model with additional UV due to outflow cavity.

The poor fit and dependence on UV irradiation of CN, HCN, and HNC we already discussed above. Their formation mainly proceeds via neutral-neutral gas-phase reactions involving light hydrocarbons like C_2H and other N-bearing species (e.g., NO). Thus the no-UV model that fails to fit CN, HCN, and HNC data is also not able to fit the C_2H observed abundances.

The modeled CS abundance profile shows a poor fit to the data as well. As we also mentioned above, this is due to general lack of predictive power of modern astrochemical models for S-bearing species. Still, H_2S modeled values are in good agreement with the observed data.

The observationally-driven H_2CO abundances are only well reproduced in the outer envelope at $r > 3 \times 10^{16}$ cm, and are lower than the observed values by up to 3-5 orders of magnitude in the inner part. This is also likely caused by the same approximation of the outflow and UV-irradiated outflow cavity walls in our 1D chemical model as for CO. Alternatively, our observations may lack the necessary resolving power and sensitivity to uncover and unbiasedly constrain the underlying physical structure of the inner NGC 1333 IRAS 4A envelope, which comes out in the lack of agreement between the data and the chemical predictions. The similar behaviour is shown by H_2CO isotopologues and chemically-related methanol molecule.

In Figures 5.17–5.19 we show the effect of including an additional UV component into the chemical model, as our attempt to represent the UV-irradiated outflow cavity material. As we discussed above, additional UV radiation lowers the degree of CO depletion and brings us much closer to agreement between the observed and modeled CO abundances. The same effect is seen for our N-bearing species (CN, HCN, HNC). Unfortunately, for all other observed species (HCO^+, N_2H^+, CS, H_2CO isotopologues, CH_3OH, C_2H, S-bearing species) the modeled abundance profiles have poorer agreement with observations than in the standard model. The enhanced UV irradiation makes too rapid destruction of less tightly bound molecules than CO, plus it limits the efficiency of surface chemistry by desorbing ices too efficiently. The potential solution to such a chemical discrepancy is to perform chemical modeling using a more realistic 2D or 3D physical structure of the NGC 1333 IRAS 4A envelope, including the outflow and outflow cavity wall and performing UV radiative transfer.

Time dependency and different input parameters

Our models are time dependent so we also investigate the influence of different timescales on the produced chemical abundance profiles. Figure 5.20 in the appendix presents the time dependent abundance profiles of several species, demonstrating the insignificant influence of time in the short timescales that characterize a Class 0 object (10^4-10^5 yrs). Our observed methanol abundance though is in better agreement with the modeled methanol

abundance for $\geqslant 4\times10^4$ yrs (Figures 5.15, 5.20), while other species do not show significant abundance variation on these timescales and thus we cannot use them as additional constraints for the age. We provide a lower limit to the age of IRAS 4A which is at least 4 times older than the one given by Maret et al. (2002) and potentially in agreement with the value of 9×10^4 yrs given by Gonçalves et al. (2008) based on the morphology of the observed magnetic field. We should point out that the derived best–fit age of our object is dependent on the framework of model that we use. If in reality conditions are different (e.g. different physical structure) or our chemical network misses some key reactions the best-fit age value can vary significantly. A rigorous way to do such modeling would require running numerous models with varying T, ρ, CR ionization rate, and reaction rates, which would give a best–fit chemical age plus its error bars. A previous study towards young high-mass star-forming regions took these factors into account and found chemical ages that were characterized by uncertainties of a factor of 2–3 (Gerner et al. 2014).

To test the dependence of our results on the adopted physical conditions, we have run models with a 2 times higher cosmic ray ionization rate, a grain growth up to 0.5 μm and different initial abundances for timescales between 10^3 and 10^6 yrs. To set the different initial abundances for the chemical modeling, we calculated the chemical evolution of a 0D model of an Infrared Dark Cloud with $n_H = 2\times 10^5$ cm^{-3}, T = 15 K, $\zeta_{CRP} = 5\times10^{-17}$ s^{-1}, H_2 OPR = 3:1 and A_V = 10 mag over 1 Myr. The neutral "low metals" elemental abundances of Graedel et al. (1982) and Agúndez & Wakelam (2013) were used. The resulted abundance profiles of this process can be seen in Figure 5.21.

We find that the CO abundance profiles are not affected strongly by increasing the cosmic ray ionization rate. In contrast, the model with bigger grain sizes of 0.5 μm shows an increase in CO abundances by 1–2 orders of magnitude at the snowline. This is because the total dust surface area per unit gas volume is smaller in this model compared to the standard case of 0.1 μm grains, lowering the pace and hence the degree of the CO freeze out. The effect is particularly dramatic at shorter chemical ages of $\sim 10^3$ years, where the difference in CO abundances between the 0.1 μm and 0.5 μm models is $\sim 3-4$ orders of magnitudes. Lastly, we find that the different initial abundances can cause a decrease of 1–2 orders of magnitude in the abundance profiles at the inner or outer envelope but does not significantly affect the CO abundance at the snowline. Only in combination with the short timescale of 10^3 yrs do we see 0.5–1 order of magnitude higher abundance at the snowline compared to the other timescales.

5.7 Conclusions and discussion

We used HIFI and JCMT data to constrain the chemical structure of a low mass protostellar envelope and compare it with a high mass equivalent.

- The empirical abundance profiles for most species appear to match the modeled chemical abundances in the outer envelope.

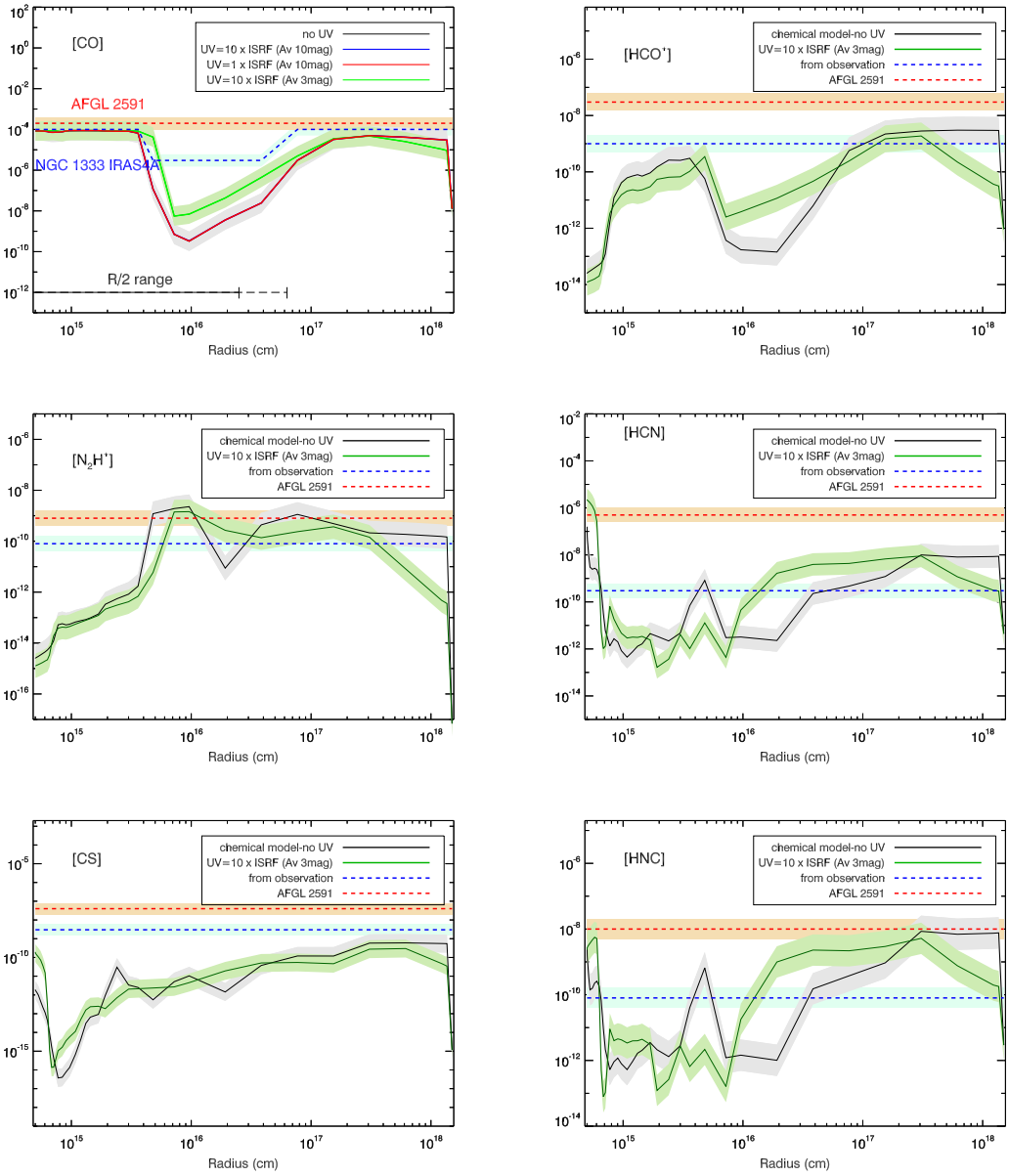

Figure 5.14: Observed and modeled abundance profiles of CO, HCO^+, N_2H^+, CS, HCN and HNC at the minimum representative timescale of 4×10^4 yrs as predicted from the time dependent CH_3OH models. The red dashed lines show the abundance profile of the outer envelope of the high–mass case, AFGL 2591 (Kaźmierczak-Barthel et al. 2015) for comparison with NGC 1333 IRAS 4A (blue). The black solid lines represent the abundance profiles from the 1D chemical model. The green solid lines represent the abundance profiles from the 1D chemical model that aim to take into account outflow cavities by applying an extra UV radiation of 10×ISRF at A_V=3 mag. The angular resolution of the observations vary between ∼15″ and ∼35″, which corresponds to 2.5 – 6.3 × 10^{16} cm in the models.

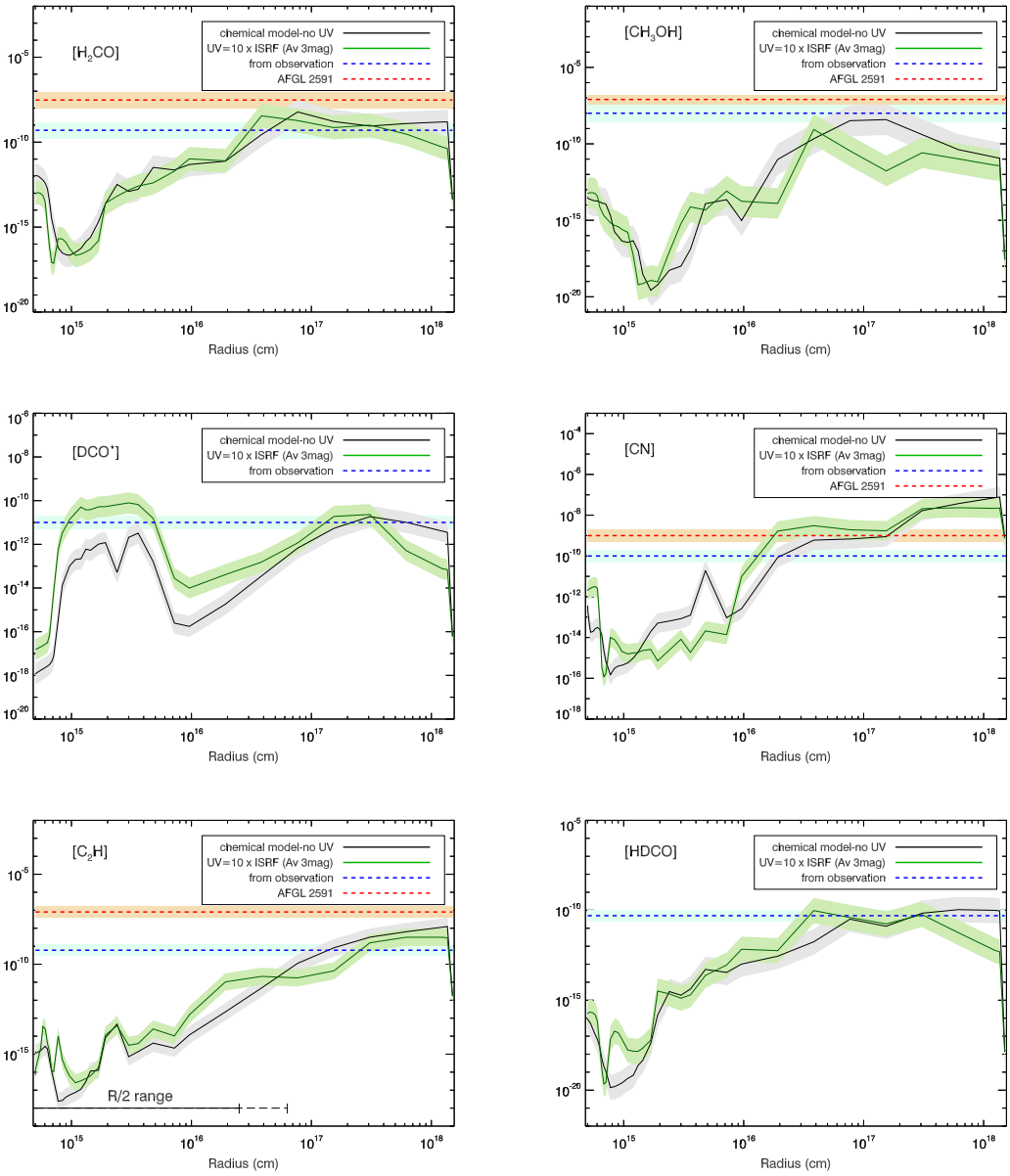

Figure 5.15: As Fig. 5.14, but for H_2CO, CH_3OH, C_2H, CN, HDCO, CO and DCO^+. The deuterated species, HDCO and DCO^+ were not observed towards AFGL 2591.

- The empirical abundance profiles for the low mass protostellar envelope (NGC 1333 IRAS 4A) are systematically 1 to 2 orders of magnitude lower than the high mass protostellar envelope (AFGL 2591).

- The population diagrams of H_2CO do not show a significant difference regarding the excitation conditions among the envelope and the outflow.

- High D_2CO over H_2CO ratio (10%) points towards formation via grain surface reactions during the cold phase and not gas–phase chemistry. This is in agreement

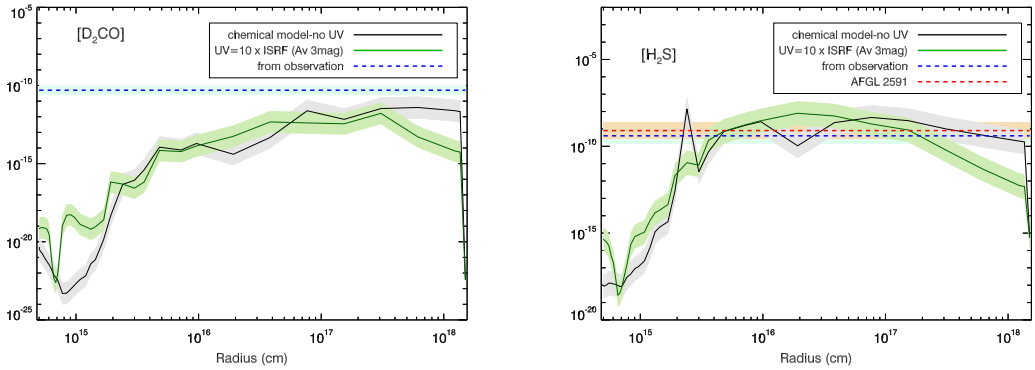

Figure 5.16: As Fig. 5.16, but for H_2S and D_2CO. D_2CO was not observed towards AFGL 2591.

with what is has been observed before towards IRAS 16293-2422.

- H_2D^+ shows a different spatial distribution compared to the other deuterated species and a peak velocity at $\sim$8 km s^{-1}. The most prominent explanation is that it is located in a different layer of gas than the clump that contains the protostars.

- The abundance profile of CH_3OH provides a lower limit for the age of NGC 1333 IRAS 4A of 4×10^4 yrs.

The modeled chemical abundance profiles of the inner envelope are a few orders of magnitudes lower than the observed ones for all species. More transitions of the observed species will help us in the future to better constrain the observed profile. We tried to simply simulate an outflow cavity by increasing the UV radiation that the observed species were exposed to. We found that this approach improved the fit among the theoretical abundance profiles and the observed, thus a more detailed 2D/3D chemical modeling that takes into account disk structure and outflow cavities is expected to be more accurate. We attribute the observed abundance difference among the low and the high mass protostellar envelope to the higher temperatures that characterise the high mass case and the absence of the freeze–out zone.

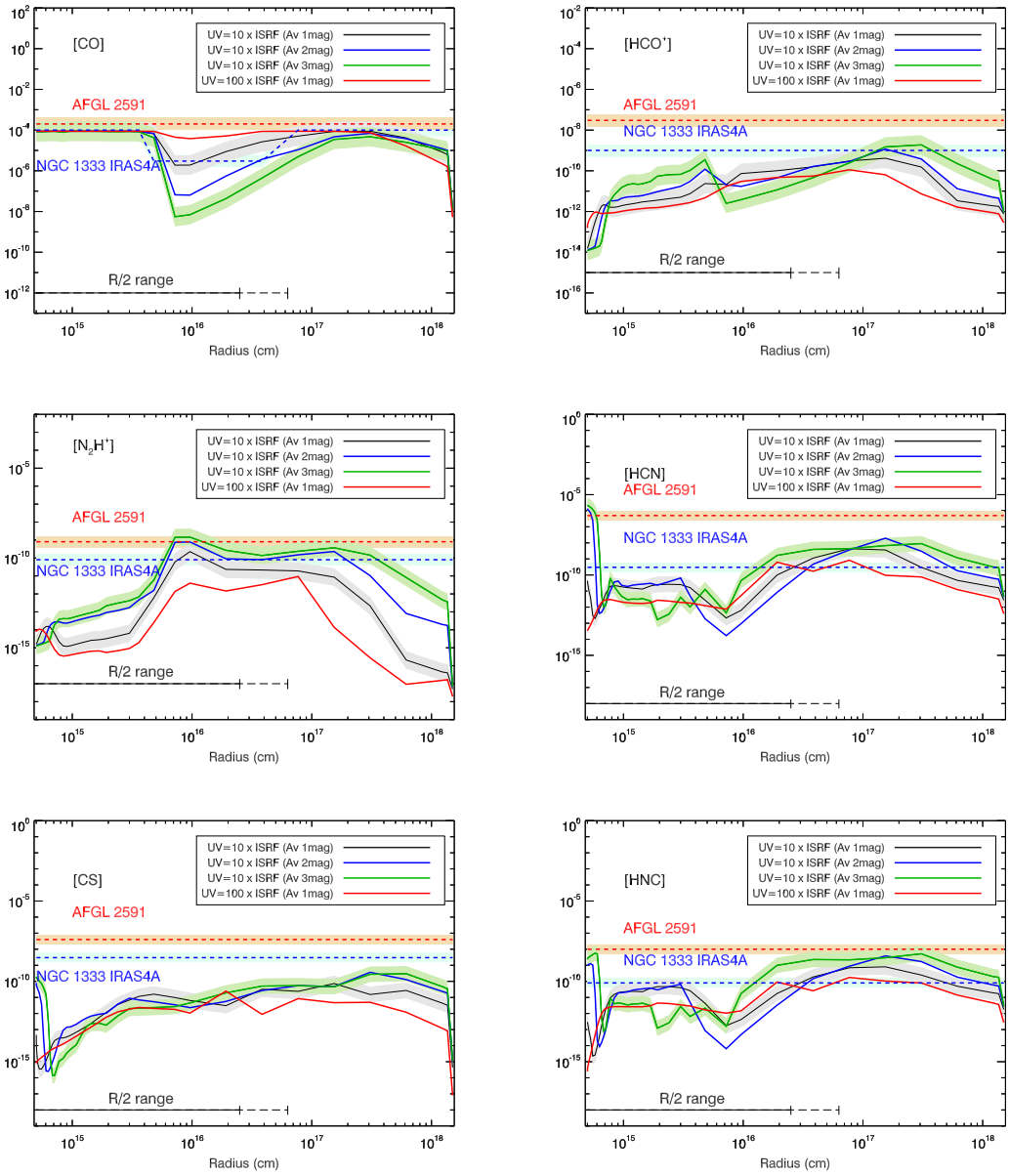

Figure 5.17: Observed and modeled abundance profiles of CO, HCO^+, N_2H^+, CS, HCN and HNC at the minimum representative timescale of 4×10^4 yrs as predicted from the time dependent CH_3OH models. The red dashed lines show the abundance profile of the outer envelope of the high–mass case, AFGL 2591 (Kaźmierczak-Barthel et al. 2015) for comparison with NGC 1333 IRAS 4A (blue). The solid lines represent the abundance profiles from the 1D chemical model applying an extra UV radiation of $10\times$ISRF A_V=1mag, 2mag and 3mag, and the extreme case of $100\times$ISRF and A_V=1mag. The angular resolution of the observations vary between $\sim15''$ and $\sim35''$, which corresponds to $2.5 - 6.3 \times 10^{16}$ cm in the models.

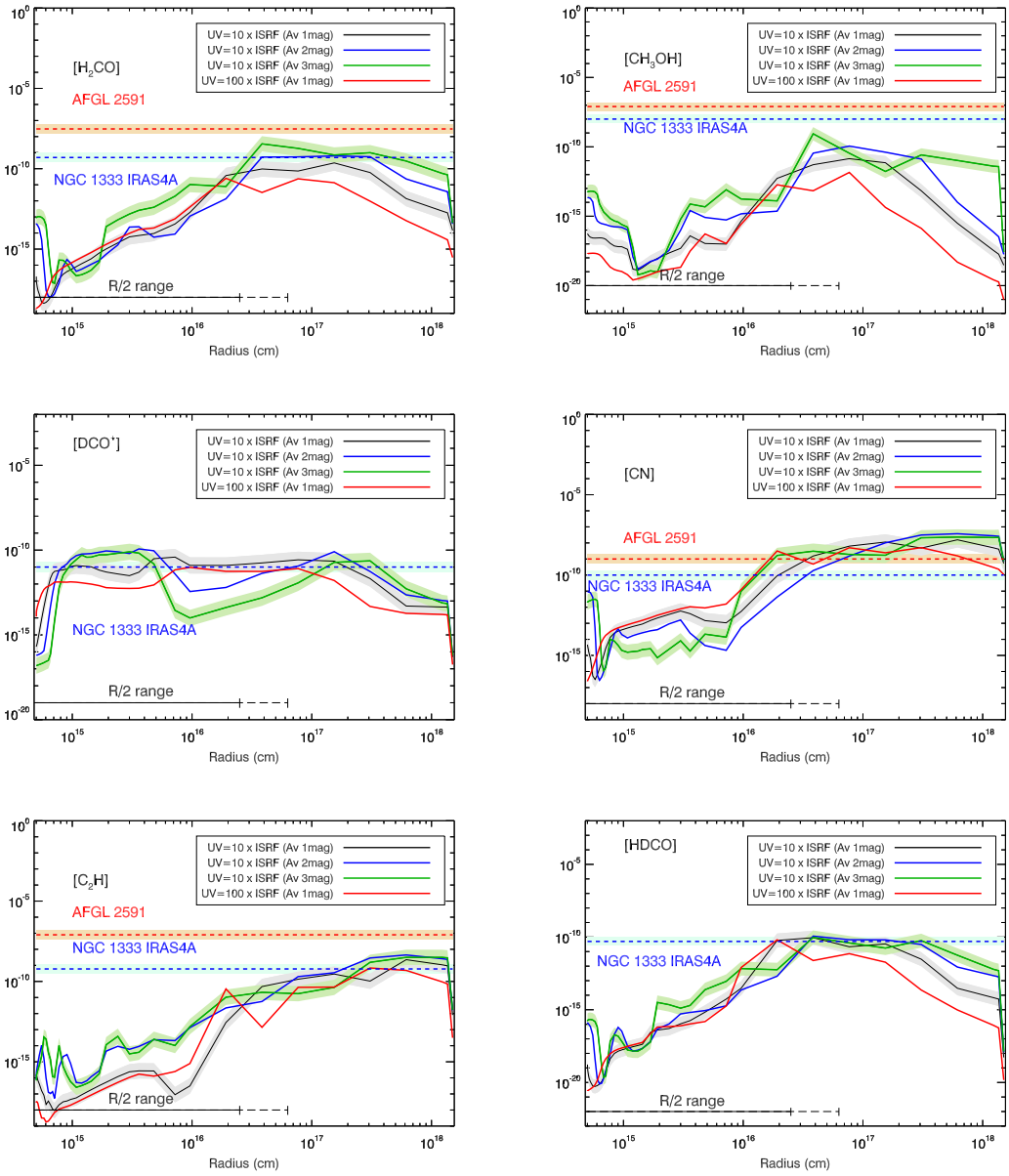

Figure 5.18: As Fig. 5.17, but for H_2CO, CH_3OH, C_2H, CN, HDCO, CO and DCO^+. The deuterated species, HDCO and DCO^+ were not observed towards AFGL 2591.

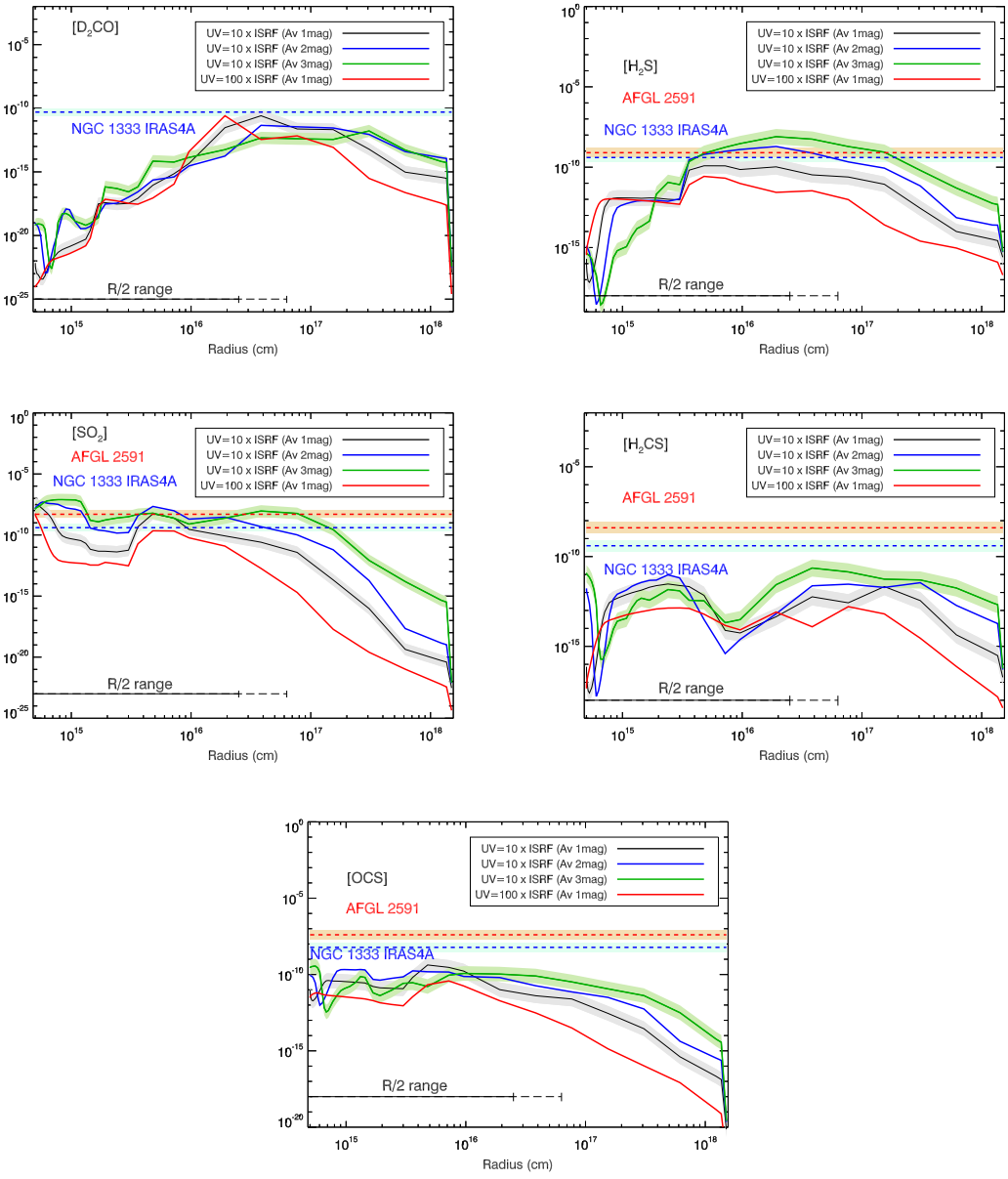

Figure 5.19: As Fig. 5.17, but for H_2S, D_2CO, SO_2, H_2CS and OCS. D_2CO was not observed towards AFGL 2591.

5.A Line detections towards NGC 1333-IRAS 4A

Table 5.6: Molecular Line Detections for NGC 1333-IRAS 4A - HIFI data

				Broad component			**Narrow component**		
Molecule	Transition	Rest Frequency (MHz)	E_{up} (K)	V_{lsr} (km s^{-1})	FWHM (km s^{-1})	T_A^* (K)	V_{lsr} (km s^{-1})	FWHM (km s^{-1})	T_A^* (K)
CO	6-5	691473.08	116.2 shows absorption						
^{13}CO	6-5	661067.28	111.0	6.7 ± 0.1	10.7 ± 0.4	0.19 ± 0.01	6.93 ± 0.01	1.60 ± 0.04	0.74 ± 0.01
^{13}CO	7-6	771184.12	148.1	7.4 ± 0.3	9.0 ± 1.0	0.17 ± 0.02	6.78 ± 0.03	1.4 ± 0.1	0.48 ± 0.03
C^{18}O	6-5	658553.28	110.6	6.8 ± 0.1	2.4 ± 0.3	0.14 ± 0.02	6.81 ± 0.05	0.6 ± 0.2	0.11 ± 0.03
HCO$^+$	8-7	713341.23	154.1	6.1 ± 0.6	7.0 ± 2.0	0.17 ± 0.04	7.07 ± 0.04	1.9 ± 0.1	0.68 ± 0.05
N_2H^+	7-6	652095.57	125.2	7.7 ± 0.2	5.3 ± 0.3	0.05 ± 0.08	7.5 ± 0.1	1.5 ± 0.4	0.15 ± 0.08
N_2H^+	8-7	745209.87	161.0	7.9 ± 0.1	2.3 ± 0.3	0.13 ± 0.02	7.73 ± 0.05	0.5 ± 0.10	0.11 ± 0.02
H_2O	2(1,1)-2(0,2)	752033.14	136.9	8.6 ± 0.6	30.2 ± 0.7	0.34 ± 0.01	0.2 ± 0.2	11.4 ± 0.9	0.24 ± 0.02
HCN	8-7	708877.21	153.1	6.4 ± 0.5	8.9 ± 0.5	0.10 ± 0.01			
HCN	9-8	797433.66	191.4	4.7 ± 0.6	6.4 ± 0.6	0.09 ± 0.01			
CS	13-12	636531.84	213.9	6.8 ± 0.5	6.2 ± 0.5	0.05 ± 0.02			
CS	14-13	685434.76	246.8	4.5 ± 0.5	6.2 ± 0.5	0.05 ± 0.2			
CS	15-14	734324.00	282	5.5 ± 0.6	6.1 ± 0.6	0.04 ± 0.01			
H_2S	2(1,2)-1(0,1)	736034.10	55.1	6.6 ± 0.1	0.5 ± 0.1	0.4 ± 0.1	6.9 ± 0.2	4.1 ± 0.2	0.13 ± 0.01
H_2CO	9(1,9)-8(1,8)	631702.81	163.6	8.0 ± 0.2	2.7 ± 0.3	0.18 ± 0.02			
H_2CO	9(0,9)-8(0,8)	647081.73	156.2	6.5 ± 0.2	3.8 ± 0.5	0.09 ± 0.01			
H_2CO	9(5,5)-8(5,4)	655212.10	451.2	6.2 ± 0.2	2.8 ± 0.6	0.08 ± 0.02			
H_2CO	9(1,8)-8(1,7)	674809.78	174.0	6.3 ± 0.2	4.6 ± 0.6	0.13 ± 0.01			
H_2CO	10(1,10)-9(1,9)	701370.46	197.3	6.9 ± 0.1	4.7 ± 0.2	0.19 ± 0.01			
CH_3OH	5(-2,4)-4(-1,4)	665442.45	60.7	6.5 ± 0.8	5.2 ± 0.8	0.05 ± 0.01			
CH_3OH	4(2,3)-3(1,2)–	673745.93	60.9	6.9 ± 0.4	4.2 ± 0.4	0.07 ± 0.03			
CH_3OH	8(1,8)-7(0,7)++	674990.42	97.4	5.9 ± 0.3	5.0 ± 0.3	0.09 ± 0.01			
CH_3OH	4(2,2)-3(1,3)++	678785.45	60.9	6.6 ± 0.5	6.1 ± 0.5	0.05 ± 0.01			
CH_3OH	9(1,9)-8(0,8)++	719664.88	118.1	6.9 ± 0.2	3.7 ± 0.3	0.09 ± 0.01			
CH_3OH	5(2,3)-4(1,4)++	728862.52	72.5	5.2 ± 0.5	5.0 ± 0.5	0.07 ± 0.01			
CH_3OH	5(3,2)-4(2,2)	772453.80	82.5	6.4 ± 0.6	5.6 ± 0.6	0.05 ± 0.01			
CH_3OH	6(2,4)-5(1,5)++	779380.51	86.5	6.9 ± 0.2	1.8 ± 0.2	0.15 ± 0.01			

5.B Chemical models for various input parameters

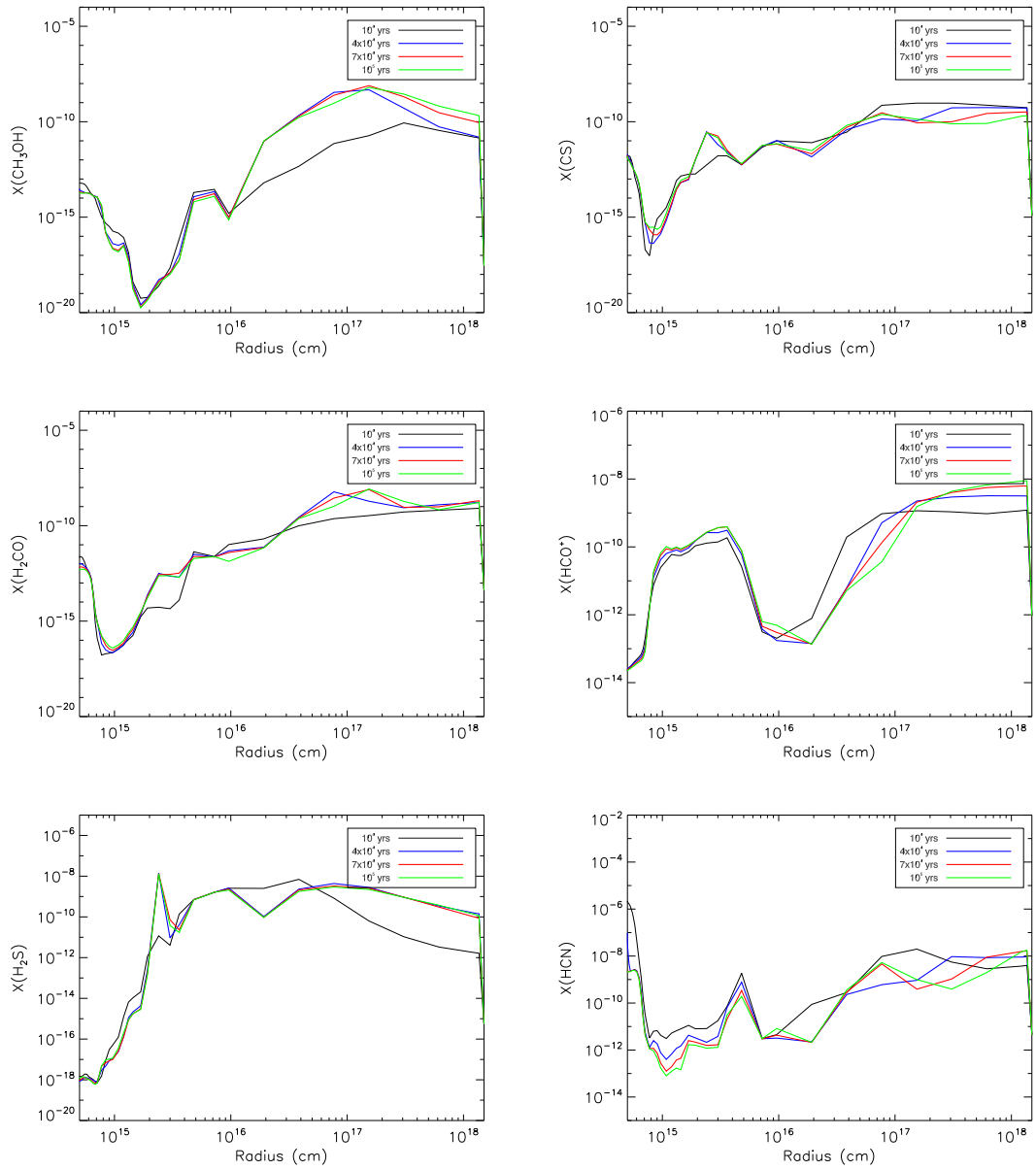

Figure 5.20: Time dependent 1D chemical models for timescales 10^4 – 10^5 yrs, which is the predicted lifespan of Class 0 objects. The observed variations are not significant and thus we adopt the 10^4 models to compare with our empirical models.

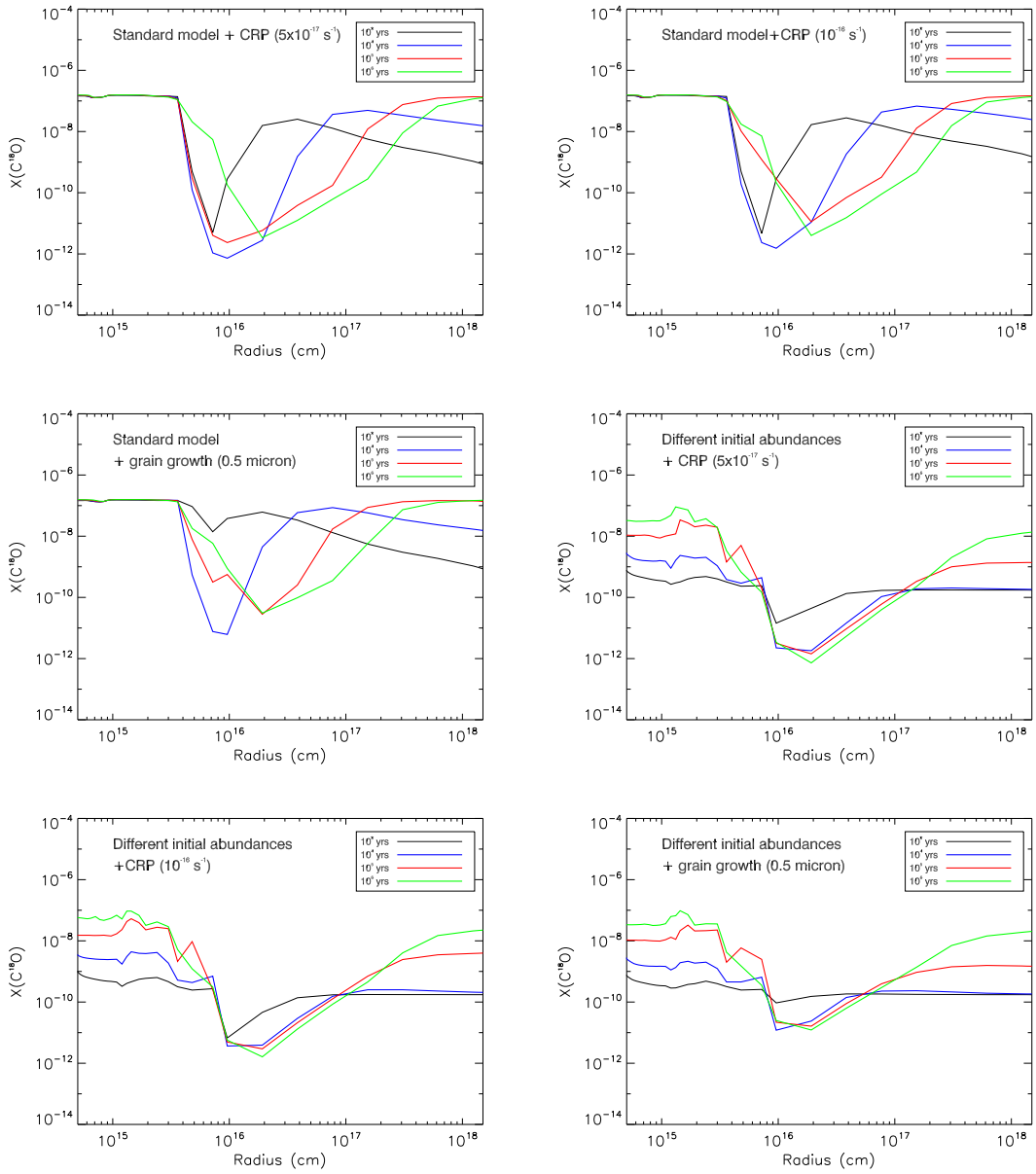

Figure 5.21: Time dependent 1D chemical models for timescales 10^3 – 10^6 yrs adopting different "extreme" inpout parameters. These models include 2 times higher cosmic ray ionization rate, a grain growth up to 0.5 μm and different initial abundances.